JOURNAL OF GUIDANCE, CONTROL, AND DYNAMICS
Vol. 41, No. 3, March 2018

Survey on Guidance Navigation and Control Requirements for Spacecraft Formation-Flying Missions

G. Di Mauro, M. Lawn, and R. Bevilacqua
University of Florida, Gainesville, Florida 32611-6250

DOI: 10.2514/1.G002868

I. Introduction

FORMATION flying (FF) has received much attention recently because of the advantages it offers in terms of mission cost, performance, and flexibility as compared with a monolithic, complex vehicle. The distribution of functions and payload among multiple spacecraft operating in a coordinated way gives the possibility to enhance the mission science return. Moreover, the use of a network of cooperative satellites increases the redundancy in the event of a failure. In light of this, different national space agencies, government research and development (R&D) centers, universities, and private companies have designed and funded more than 20 FF missions in the last two decades and plan to launch another 10 within the next nine years (see Fig. 1).

The main challenge related to spacecraft FF missions is the design of robust and reliable guidance, navigation, and control (GNC) techniques for onboard systems. Thus, the intent of this paper is to determine the state of the art of the onboard GNC system in terms of hardware/software solutions and achievable performances through a comprehensive survey of past, current, and future FF missions. Many past works focused on the review of the research status of GNC techniques [1,2]. However, an analysis of the onboard GNC systems, investigating the required/achieved performances, the functional architecture, and the onboard hardware, appears to not be available in the literature except for a specific class of spacecraft, i.e., the small satellites [3]. This survey considers missions launched between year 2000 and now, as well as future missions proposed up to year 2025 (including those that are at the preliminary prephase A design stage).

In addition, this study seeks to identify the new technological trends for FF missions and their effects on the GNC system design. To date, many missions, such as the Canadian Advanced Nanosatellite eXperiment-4 and -5 (CanX-4&5; see Sec. II.C.4) or the Project for On-Board Autonomy-3 (PROBA-3) [4], have launched or are planned to be launched to test technologies for autonomous proximity operations. In fact, a completely autonomous system guarantees superior performance in terms of control accuracy and higher mission flexibility/adaptability, providing a prompt response to contingencies. Moreover, onboard autonomy allows performing maneuvers far from Earth, overcoming problems due to large communication delays, and reducing the operations costs. This need for autonomy presents a new set of challenges in the areas of onboard sensing, actuation, and maneuver planning, as well as in mission

Dr. Giuseppe Di Mauro is a Postdoctoral Associate in the Mechanical and Aerospace Engineering Department at the University of Florida, where he works in the Advanced Autonomous Multiple Spacecraft Laboratory. He received his Ph.D. from Politecnico di Milano in aerospace engineering in 2013. Afterward, he worked as Senior Project Engineer at Dinamica Srl for three years. Dr. Di Mauro's research interests include nonlinear feedback control design and relative navigation system design.

Mrs. Margaret Lawn is a second-year graduate student in the Advanced Autonomous Multiple Spacecraft Laboratory at the University of Florida. She graduated with a B.S. in aerospace and mechanical engineering from the University at Buffalo, State University of New York, in 2015. Her research interests include multiple spacecraft guidance and control.

Dr. Riccardo Bevilacqua is an Associate Professor of the Mechanical and Aerospace Engineering Department at the University of Florida where he works in the Advanced Autonomous Multiple Spacecraft Laboratory. He holds a M.Sc. in aerospace engineering (2002) and a Ph.D. in applied mathematics (2007), both from the University of Rome "La Sapienza". Dr. Bevilacqua is the recipient of two Young Investigator Awards, from the U.S. Air Force Office of Scientific Research (2012) and the Office of Naval Research (2013); the 2014 Dave Ward Memorial Lecture Award from the Aerospace Controls and Guidance Systems Committee; and two Air Force Summer Fellowships (2012 and 2015). His research interests focus on spacecraft formation flight and space robotics. He has authored or coauthored more than 50 journal and conference publications on the topic. He is an AIAA Associate Fellow.

Received 24 February 2017; revision received 10 August 2017; accepted for publication 6 October 2017; published online 16 November 2017.

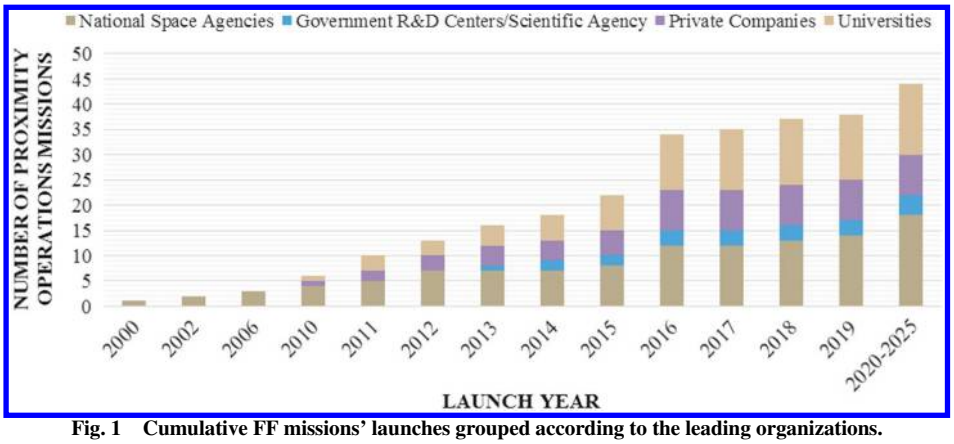

Fig. 1 Cumulative FF missions' launches grouped according to the leading organizations.

management and scheduling; monitoring; and fault detection, isolation, and recovery (FDIR). Another key aspect that should be considered in the design of GNC systems of future FF missions is the decrease of the size of the spacecraft. The use of small satellites (mass lower than 500 kg), especially nano- and microsatellites (see Table 1), is growing tremendously in the space field, thanks to the development and wide use of the CubeSat standard and all related technology equipment [5,6]. As an immediate consequence, small satellites have been increasingly proposed to build up distributed space systems for Earth observation and science purposes. However, even though the use of this class of spacecraft presents several advantages in terms of mission costs, there are additional constraints placed on the GNC system due to limited onboard resources (both thrust/power and computational capabilities). Ultimately, in recent years, FF missions have been proposed to build multiple-spacecraft space observatories operating in low-acceleration environments, i.e., sun–Earth L2 point. To accomplish their objectives, satellites have to operate at large distance while controlling their relative configuration with a high accuracy. The second important contribution of this work is therefore to trace the roadmap for GNC system design to achieve the challenges posed by these new technological trends.

The rest of the paper is organized as follows. In Sec. II, a critical analysis of FF missions is presented. These missions are classified based on their primary objective, spacecraft mass, and operating orbital regime. Within the same section, the main technological trends of future FF missions are discussed and a detailed description of a subset of missions is given, including their onboard GNC architecture (sensors, actuators, and strategies). In Sec. III, the GNC performances in terms of control and navigation accuracies are presented for each objective-related mission class and the main areas of development in GNC design are discussed.

II. Past, Present, and Future Formation-Flying Missions

A. Analysis of Formation-Flying Missions

Across the scientific community, there are numerous definitions for formation flying and related terms. In accordance with the definition given in [7], with the term "formation flying," we hereafter indicate those missions consisting of two or more satellites that have to track and maintain a desired relative trajectory and/or a relative orientation.

Table 1 Satellite platform classification based on mass

Quantity	Platform mass, kg
Large spacecraft	≥1000
Medium spacecraft	≥500 and <1000
Small spacecraft	<500
Minispacecraft	≥100 and <500
Microspacecraft	≥10 and <100
Nanospacecraft	≥1 and <10
Picospacecraft	≥0.1 and <1
Femtospacecraft	≤0.1

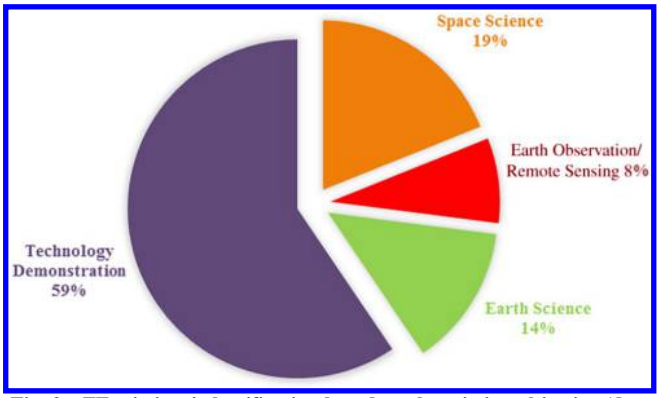

Fig. 2 FF missions' classification based on the mission objective (data from 2000 to 2025).

In this section, FF missions already launched or planned to be, spanning the space programs from 2000 to 2025 (see Appendix Table A1 for the complete list of surveyed missions), are reviewed. Note that, for the sake of a comprehensive survey, we took into account all those designed by national space agencies, government R&D centers or scientific agencies, universities, and private companies spread out all around the world. Moreover, among the future missions, we also included those that are at prephase A design stage. We classified the reviewed FF missions based on the following criteria:

1) The first criterion is mission objective. Four different primary mission objectives are considered in our study: a) space science, b) Earth observation/remote sensing, c) Earth science, and d) technology demonstrations.

2) The second criterion is the maximum mass of the spacecraft. Three satellite classes are taken into account: a) large spacecraft, b) medium spacecraft, and c) small spacecraft. A spacecraft is hereafter called a "small satellite" when its wet mass is below 500 kg. As reported in Table 1, a variety of spacecraft falls in this category, such as mini-, micro-, nano-, pico-, and femtosatellites. Moreover, in accordance with the widely accepted classification of satellites based on their mass, "medium" and "large" terms indicate those spacecraft with a wet mass larger than 500 and 1000 kg, respectively [8].

3) The third criterion is the orbital regime. Four different types of orbits are considered: a) low Earth orbits (LEOs); b) high elliptical orbits (HEOs); c) geosynchronous orbits (GEOs); and d) Lagrangian points orbits (LPOs), which are also referred to as the deep-space regime. LEOs include all Earth orbits with an apogee lower than 2000 km. HEOs indicate all Earth orbits with a high eccentricity, which is typically greater than 0.5. GEOs indicate all orbits within the segment of the spherical shell defined by an altitude range of $[-200, 200]$ km with respect to the geostationary altitude and a latitude range $[-15 \text{ deg}, 15 \text{ deg}]$ with respect to the equatorial plane. An LPO accounts for Lissajous and halo orbits around the L2 sun–Earth point.

Figure 2 shows the FF missions classification based on the mission goal. Most of them are technology demonstrators that are mainly

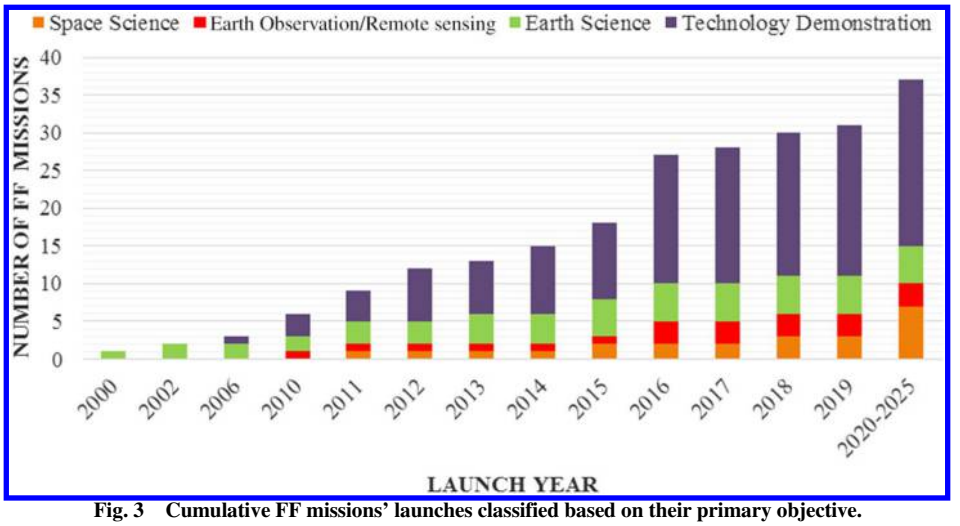

Fig. 3 Cumulative FF missions' launches classified based on their primary objective.

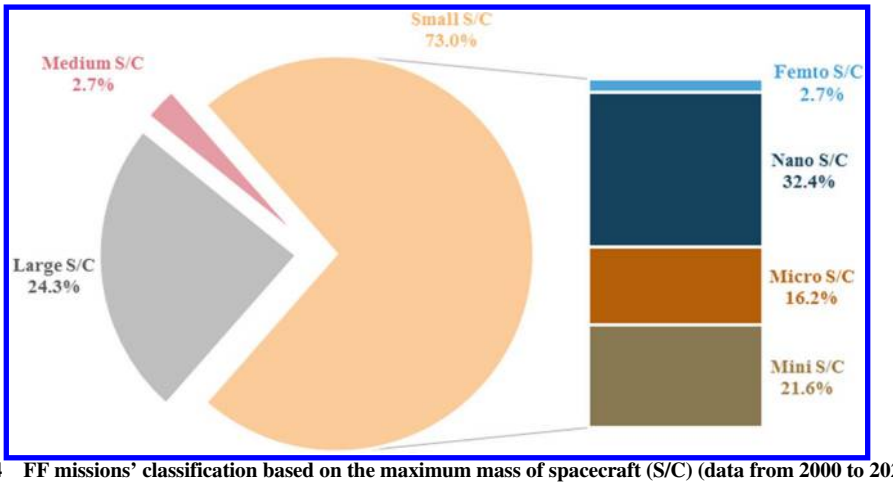

Fig. 4 FF missions' classification based on the maximum mass of spacecraft (S/C) (data from 2000 to 2025).

designed to validate the hardware and techniques needed to increase the onboard autonomy. However, a significant part of them (about 33%) is used for space and Earth science purposes.

Figure 3 shows the cumulative FF missions' launches up to 2025, classified based on their primary objective. Apparently, the percentage of missions for space science and exploration is quickly increasing (see last column in Fig. 3). In fact, multiple collaborative spacecraft are planned to be exploited to assemble telescopes for deep-space observation. As examples, it is worth mentioning two NASA missions: namely, the Exo-Starshade (EXO-S) and the Stellar Imager (SI), which are currently in a preliminary design phase and planned to be launched in 2025. The EXO-S is a space-based observatory designed to discover and study Earth-like planets. It consists of two large spacecraft, a star shade, and a science telescope* that will fly in formation in a low-acceleration environment such as the sun–Earth L2 point (halo orbit). During the science operations, the formation shall maintain lateral and longitudinal alignments within 1 m and $\pm$250 km, respectively, at separations of 30,000–50,000 km. This configuration allows the star-shade satellite, consisting of an opaque screen, to blot out the starlight, and it therefore allows the telescope to catch the exoplanet light [9]. The SI mission is an ultraviolet/optical deep-space telescope designed to image stars similar to our sun with milli-arcsecond resolution. The current baseline architecture concept consists of a 0.5 km diameter UV-optical Fizeau interferometer composed of a reconfigurable array of 10–30 1-m-class deformable flat mirror elements ("mirrorsats") and an image plane beam-combination facility placed at the prime focus of telescope ("hub"). The hub and all mirrorsats are free flyers in a tightly controlled formation operating around the sun–Earth L2 point [10].

Figure 4 illustrates the distribution of spacecraft mass for FF missions. Most of the analyzed missions involve small satellites, with a large part (about 32%) consisting of nanosatellites (1 kg $\leq$ Mass < 10 kg). Among the small-spacecraft class of FF missions, the Silicon Wafer Integrated Femtosatellites (SWIFT) project deserves attention because it is the only one (to the authors' knowledge) that involves femtosatellites (Mass < 100 g). The SWIFT mission, led by the Jet Propulsion Laboratory (JPL), the University of Illinois at Urbana–Champaign, and the Scientific Systems Company, Inc.; and funded by the Defense Advanced Research Projects Agency, aims to launch a swarm (100 to 1000 elements) of 100-g-class satellites into LEO (about 500 km) to build a huge distributed sensor network [11]. This kind of mission poses two main challenges: the miniaturization of satellite hardware (propulsion system, electronic for long-distance communication, etc.), and the development of optimal-fuel and computationally efficient GNC algorithms. Currently, advanced techniques are under investigation for GNC design, such as adaptive graph Laplacian integrated with a phase synchronization controller for the formation control, or a decentralized model predictive control/sequential convex programming algorithm and probabilistic swarm guidance for guidance definition (we refer the reader to [11] for an extensive review of GNC algorithms for the SWIFT mission). However, a significant part of FF missions (about 24%) involves large spacecraft. The presence of these massive satellites is justified by the future missions for space science in LPO that foresee the use of heavy

*The telescope spacecraft will be the Wide Field Infrared Survey Telescope. Data are available online at http://wfirst.gsfc.nasa.gov/ [retrieved 13 November 2016].

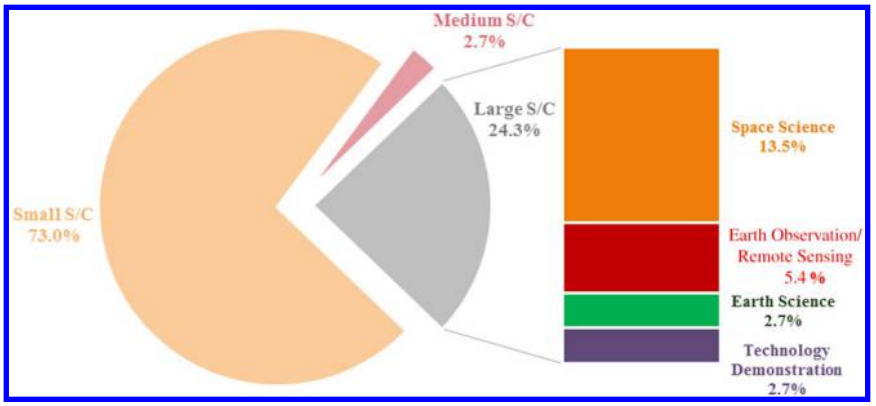

Fig. 5 Primary objectives for large spacecraft FF missions (data from 2000 to 2025).

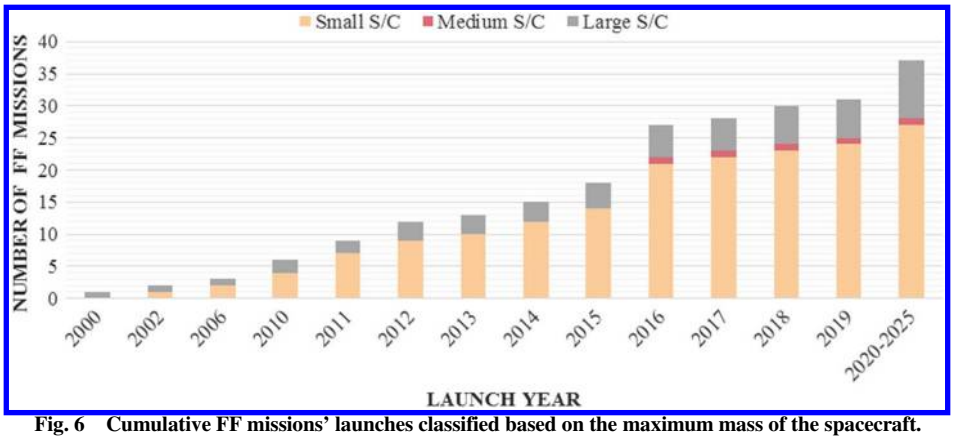

Fig. 6 Cumulative FF missions' launches classified based on the maximum mass of the spacecraft.

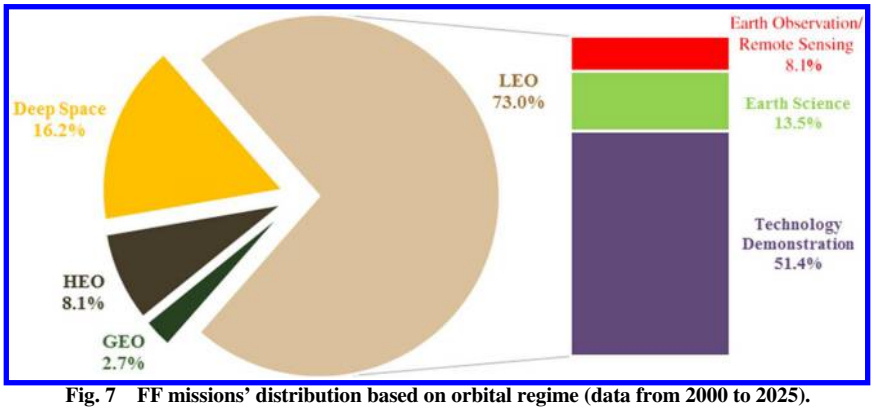

Fig. 7 FF missions' distribution based on orbital regime (data from 2000 to 2025).

platforms to host the main hardware of a distributed space-based observatory (see Fig. 5).

Figure 6 depicts the distribution of spacecraft mass throughout the past and future launches. Accordingly, future FF missions will see a further increase of small and large spacecraft for Earth science and technology demonstration and deep-space observation applications, respectively.

Ultimately, from the data collected within this survey, it turns out that most FF missions operate in the LEO regime (see Fig. 7). However let us remark that the number of missions flying on LPOs is destined to rise because this is the orbital region commonly used for deep-space observation.

B. Future of Formation-Flying Missions

The review of FF missions presented in Sec. II.A shows the growing interest of the scientific community in the increase of onboard autonomy. In fact, high onboard autonomy allows us to 1) lighten the ground stations' and control centers' operational loads, reducing the overall mission costs; 2) increase the science return by reducing the inactivity period due to the coverage problems or large communication delays; 3) facilitate the response to contingences/failures, therefore increasing the mission robustness and safety; and 4) guarantee mission flexibility/adaptability, allowing a prompt response to the environment changes.

However, the achievement of complete onboard autonomy poses a challenge in the areas of onboard sensing, actuation, and maneuver planning (i.e., GNC design), mission management and scheduling, as well as monitoring and FDIR. The development of autonomous embedded GNC systems, for instance, might affect the design of navigation and control systems as well as the maneuver planning (guidance function). Sensors for inertial and relative navigation have to provide reliable measurements, regardless of the environmental conditions; whereas the filtering and control algorithms need to guarantee a high robustness level without sacrificing the accuracy performance. On the other hand, the guidance function has to generate a solution capable of satisfying the safety and fuel consumption requirements over a large period of time, with a high computational efficiency to limit the onboard computational load. Despite the

technology challenges, the increase of onboard autonomy could be the only possible way to operate those missions flying far from the Earth, which would suffer communication delay problems; and/or involving a large number of elements, which would imply high operational complexity and prohibitive costs, such as the future missions of SWIFT [11] or space ultra-low frequency radio observatory (SULFRO) [12]; as well as requiring high control accuracy.

In addition, the analysis of future missions points out the other two critical aspects affecting the GNC system design: 1) the need to increase the GNC performance, and 2) the decrease of spacecraft size.

Future FF missions will require a higher dynamic range ($\approx 10^8$), defined as the ratio between the mean intersatellite distance and the required control accuracy [13]. In other words, they will need a high intersatellite distance (≈1001–10,000 km) coupled with a moderate control accuracy (≈0.001–0.1 m) or an extremely high control accuracy (≈10–100 μm) coupled with a moderate relative distance (≈1–10 km). To meet this demanding control requirement, more efficient control techniques shall be developed to run on board, such as an optimal nonlinear model-based controller able to account for dynamical nonlinearities.[†] As an immediate consequence of the growing dynamic range requirement, there is the need for higher relative navigation accuracy. To this purpose, more accurate relative dynamics models shall be developed to improve the performance of the filtering process in terms of accuracy and computational load.

The last key aspect to be taken into account is the reduction of the satellite dimension. Small satellites have been increasingly proposed, mainly to validate new technology in orbit; however, in the future, they will be used to build up distributed space instruments for Earth and deep-space observation. As an example, it is worth mentioning the Miniaturized Distributed Occulter Telescope (mDOT) mission, which a space telescope designed by the Space Rendezvous Laboratory (SLAB) at Stanford University, consisting of a microsatellite carrying a 1–2-m-radius petal-shaped occulter at a distance lower than 1000 km from a 6 Unit CubeSat carrying a 10-cm-diam aperture telescope to image at short visible and ultraviolet wavelengths [14]. Despite the benefits in terms of mission costs, the use of such small satellites presents a new set of GNC design challenges, mainly related to the vehicles' limited size and onboard power. The ability to carry a complex propulsion system able to provide high thrust is extremely limited due to the spacecraft's prohibitive dimensions. In light of this, ad hoc relative orbit control techniques, such as combined continuous and impulsive orbital control based on the optimal control theory and primer vector approach [15], shall be developed to satisfy the low-thrust constraints without renouncing the high-accuracy performance.

C. Missions Overview

In this section, we briefly describe the configuration of some of reviewed FF missions, particularly focusing on the GNC architecture. For brevity, we detail only one mission for each objective-related class presented in the Sec. II.A, i.e., space science [e.g., Magnetospheric Multiscale (MMS)], Earth observation (e.g., TanDEM-X), and Earth science [e.g., Gravity Recovery and Climate Experiment (GRACE)]. Moreover, in order to offer a better insight into state of the art of formation-flying technologies, we present three technology demonstration missions, focusing on those that allow testing onboard autonomy and validating cutting-edge solutions for the GNC system in terms of hardware (propulsion system, sensor for relative navigation) and algorithms [e.g., CanX-4&5, Bi-spectral InfraRed Optical System (BIROS)/Autonomous Vision Approach Navigation and Target Identification (AVANTI), and Prototype Research Instruments and Space Mission Technology Advancement (PRISMA)].

1. *Gravity Recovery and Climate Experiment*

The Gravity Recovery and Climate Experiment is a two-satellite mission developed by NASA and DLR, German Aerospace Center; and it was launched in March 2002. Its main objective is to map with high accuracy the spherical harmonic coefficients of Earth's gravitational field and to observe its temporal variations, measuring the separation between the two twin satellites (487 kg) using the Global Positioning System (GPS) and K-band radar ranging. Both of the identical GRACE satellites (namely, GRACE1 and GRACE2) were placed in the same circular polar orbit ($i = 89$ deg) at an altitude of 490 km. The satellites are equipped with a BlackJack GPS onboard receiver for precise orbit determination, a superspace triaxis accelerometer for research missions (known as SuperSTAR) [16], a highly accurate intersatellite K-band microwave ranging instrument [17], and an attitude control system that includes a star camera, gyroscope sensors, and a cold gas nitrogen microthruster system including two 40 mN orbit control thrusters and 1210 mN attitude thrusters [18].

a. Navigation Solution. The navigation computation is performed on ground using the GPS measurements. More specifically, the spacecraft two-line elements (TLEs) are generated on ground by fitting the simplified general perturbations (SGP)4 model to GPS measurements through a least-square method. The TLEs are sent to both spacecraft, which use orbit information to point the K-band radar at one another [19].

b. Formation Control and Guidance Solutions. Both GRACE spacecraft are ground controlled [19]. During the science data collection, the satellites are held in a three-axis stabilized, nearly Earth-pointed orientation, where the K-band antennas of each satellite are pointing at each other [17]. Station-keeping maneuvers are performed over the life of the mission to correct the alongtrack drift, and then keep the satellites within a 170–270 km separation. The alongtrack separation ΔL is analytically estimated through the following formula [20]:

$$\Delta L(t) = L(t) - L_0 = \frac{3}{4}\frac{1}{\Delta B \rho a^2}\Delta a(t)^2 \tag{1}$$

where ρ is the atmosphere density, a is the leader semimajor axis, Δa is the difference of the mean semimajor axis between the leader and follower orbits, and ΔB indicates the difference in the ballistic coefficient. According to Eq. (1), the alongtrack separation changes quadratically with the difference of the mean semimajor axis. To maximize the time between subsequent formation-keeping maneuvers, the relative altitude versus relative separation has to be a parabola mirrored to the altitude of the reference satellite (see Fig. 8). Thus, once the two spacecraft are placed at the maximum desirable separation with a semimajor axis offset $\Delta a_{\max} = \sqrt{4/3\Delta B \rho a^2 \Delta L_{\max}}$ [see Eq. (1)], a new alongtrack impulsive maneuver ($v_t = n/2\Delta a_{\max}$) is performed when $\Delta a = 0$ to raise the semimajor axis of the leading satellite or, alternatively, to lower the semimajor axis of the trailing one. $\Delta L_{\max}$ indicates the size of station-keeping box, and it is 100 km at most, in accordance with mission requirements.

The period between two subsequent maneuvers is estimated by [20]

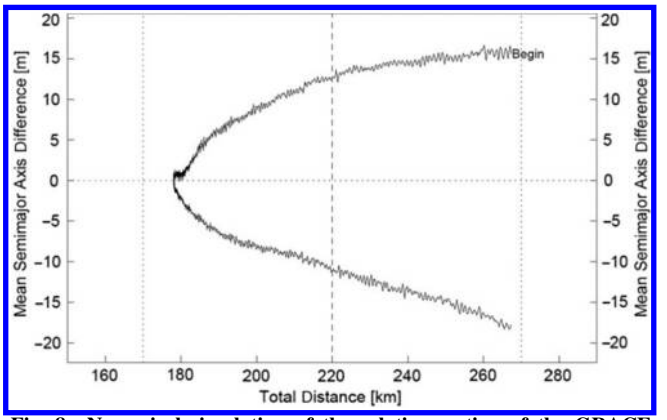

Fig. 8 Numerical simulation of the relative motion of the GRACE spacecraft under the influence of differential drag [19].

[†]To the authors' knowledge, many nonlinear optimal controllers have been studied for FF applications, but they have never been implemented on board.

$$\Delta t = \sqrt{\frac{16}{3}\frac{\Delta L_{\max}}{\Delta B \rho a^2 n^2}} \tag{2}$$

where n is the mean motion of the leader spacecraft. The preceding approach for formation maintenance is based on the assumptions of constant density and different ballistic coefficients. However, the real relative motion is perturbed by the density variation and by the change of ΔB due to the spacecraft mass variation and relative satellites' orientation, as illustrated in Fig. 8. In this figure, the relative motion of the GRACE spacecraft after the separation from the breeze upper stage is numerically simulated by taking into account the variations of density due to the realistic solar flux profiles and the changes of ballistic coefficients due to the variations of pitch angles [19].

In light of the aforementioned, the admissible station-keeping box is not entirely used in order to account for unpredictable density variations. In addition, throughout the mission, the relative distance and semimajor axis difference are monitored, as well as the evolution of the mass of both satellites. In parallel, the flight dynamics group carried out predictions of the expected motion in the L–Δa plane to decide on a suitable maneuver time and size. These predictions are carried out by considering the solar flux values and their uncertainties provided by the European Space Operations Center on a daily and monthly basis [19]. It is worth noting that the used approach is based on the knowledge of the mean orbital elements of satellites. The osculating-to-mean conversion is performed using a combination of numerical and analytical techniques to guarantee an accuracy of 1 m at least [20]. In further details, the spacecraft's trajectories are numerically integrated over a time interval of six orbits using a high-fidelity dynamics model and initial conditions from the latest orbit determination. Using a sampling interval of 10 min, the resulting state vectors y are fit to the SGP4 model by the least-square method.

Besides the formation-keeping maneuver, a maneuver exchanging the position of the satellites (i.e., longitude swap maneuver) is performed to balance the surface erosion of the antennas of the K-band ranging system caused by the exposure to the impacting atomic oxygen. In fact, an overexposure to atomic oxygen might lead to a loss of thermal control over the K-band horn antenna, which would affect the accuracy of ranging system [21]. Hence, the swap maneuver guarantees the uniform deterioration of the spacecraft K-band antennas by placing the follower spacecraft GRACE2, initially flying with the antenna exposed to the impacting atomic oxygen, beyond the leader satellite GRACE1. To obtain the desired positive alongtrack drift, the semimajor axis of the trailing spacecraft GRACE2 is modified through a tangential maneuver. To maximize the operational safety of the satellite swap maneuver with no increase in fuel expenditure, eccentricity/inclination (e/i) vector separation is applied [21]. This technique, originally developed for the colocation of geostationary satellites, guarantees a radial or crosstrack position offset between two spacecraft (the maximum offset is achieved when the relative eccentricity and inclination vectors are parallel or antiparallel), regardless of their alongtrack separation. In addition to the safety benefits, the e/i vector separation allows us to swap the GRACE satellites through a single maneuver, reducing the operational complexity. A detailed description of the swap maneuver performed in early December 2005 is given in [19,21,22].

2. *TanDEM-X (with TerraSAR-X)*

TerraSAR-X add-on for Digital Elevation Measurement (TanDEM-X), which launched in June 2010, is a digital elevation measurement science extension to the TerraSAR-X mission developed by DLR, German Aerospace Center (DLR); EADS Astrium, GmbH; and Infoterra, GmbH. The mission objective is the generation of a global high-precision digital elevation model (DEM). Depending on the interferometric configuration, the TerraSAR-X and TanDEM-X satellites fly in one of three modes: 1) bistatic mode, where both spacecraft look at the same area of the Earth to provide a detailed multidimensional picture; 2) pursuit monostatic mode, where both satellites image the same area independently at a time offset; and 3) alternating bistatic mode, which is similar to bistatic mode, except that the transmitter is switched from pulse to pulse between the satellites. The TerraSAR-X spacecraft moves on a sun-synchronous dawn–dusk orbit ($i = 97.44$ deg) at the mean altitude of 515 km with an 11-day repeat cycle.

The concept of e/i vector separation is used for the design of formation (see next subsection). This implies maximum out-of-plane (crosstrack) orbit separation at the equator crossings by small ascending node differences and maximum radial separation at the poles by slightly different eccentricity vectors. This concept of relative e/i vector separation results in a helical relative movement of the satellites along the orbit and provides a maximum level of passive safety in the case of vanishing alongtrack separation. Both spacecraft are built using the AstroBus[‡] service module and are equipped with an radar instrument. In addition, they host on board one dual-frequency tracking, occultation, and ranging/integrated GPS occultation receiver (TOR-IGOR) receiver to determine the baseline with an accuracy of 1 mm and one single-frequency EADS Astrium Mosaic global navigation satellite system (MosaicGNSS) receiver used by the navigation system [23]. TanDEM-X has also an S-band receiver to receive telemetry information from TerraSAR-X. The propulsion system for orbit maintenance maneuvers of both satellites consists of two branches of four 1 N hydrazine monopropellant thrusters. TanDEM-X is additionally equipped with four pairs of 40 mN nitrogen cold-gas thrusters oriented in the flight and antiflight directions for formation keeping [24].

a. Navigation Solution. Both satellites are equipped with three GPS receiver units: i.e., a redundant pair of single-frequency MosaicGNSS receivers that provides the time synchronization and real-time GPS navigation solution for the attitude and orbit control system, and one dual-frequency TOR-IGOR for rapid orbit determination (ROD), precise orbit determination (POD), and baseline reconstruction. The MosaicGNSS data and associate navigation solutions are also used for the real-time relative navigation during the TanDEM-X Autonomous Formation Flying experiment [25]. The TOR-IGOR data are preprocessed to extract the GPS navigation data and raw data (i.e., carrier phase and pseudorange) that are used for ROD and POD processes, respectively. In further details, the ROD performs a least-squares batch adjustment of the position and velocity, drag coefficient, solar radiation coefficient, extended maneuvers, and measurement biases, providing the quick-look orbit product with a 3 m accuracy (1σ) [26]. The corresponding orbit product is used for formation monitoring and control purpose.The POD gives the "science" orbit product through a reduced-dynamics batch least-squares estimation process [27] with an accuracy of 5 cm (1σ) [25]. Within the POD process, auxiliary data are required such as GPS satellite orbits and clocks, Earth orientation parameters, and spacecraft attitude information. The dynamic orbit model used in POD includes relevant gravitational (University of Texas/Center for Space Research GRACE Gravity Model 01S model, relativity solid-Earth tides, pole tide, ocean tides, and lunisolar third-body acceleration using analytical ephemerides) and nongravitational forces, such as atmospheric drag (Jacchia–Gill atmospheric density model with daily $F_{10.7}$ and 3 h K_p [25]). Moreover, in accordance with the concept of reduced-dynamic orbit determination, empirical acceleration in radial, tangential, and normal directions are incorporated to account for deficiencies of the deterministic force model.

The baseline estimation is carried out at DLR/German Space Operations Center (GSOC) using the Filter of Relative Navigation of Satellites (FRNS) software and at the German Research Centre for Geosciences using Bernese [28] and Earth Parameter and Orbit System-Orbit Computation software [29]. All of the aforementioned solutions are combined in order to reduce the stochastic errors inherent to all individual solutions, giving a merged baseline estimate with an accuracy of 1 mm three-dimensional rms. The aforementioned FRNS software implements an extended Kalman filter/smoother to accurately determine the relative motion of TerraSAR-X and TanDEM-X, and it uses dual-frequency double-difference carrier-phase measurements and integer ambiguity resolution [25,30].

[‡]Data available online at http://space.airbus.com/portfolio/earth-observation-satellites/portfolio/ [retrieved 13 November 2016].

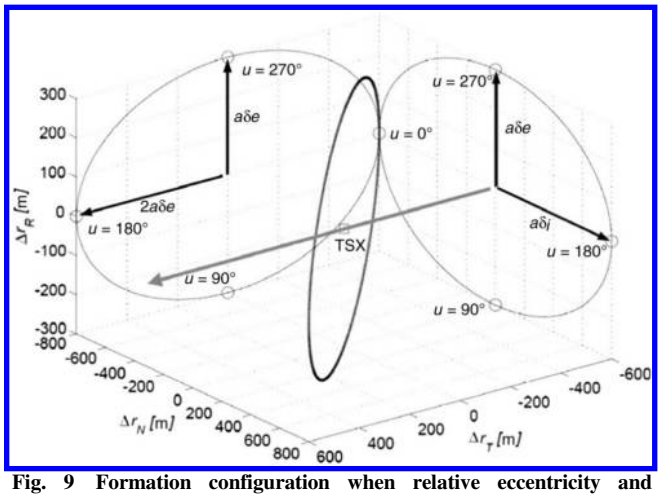

Fig. 9 Formation configuration when relative eccentricity and inclination vectors are parallel [31].

b. Formation Control and Guidance Solutions. The formation acquisition and maintenance maneuvers are exclusively performed by the TanDEM-X satellite. Both spacecraft must perform the same orbital maneuvers to counteract lunisolar perturbations and to compensate atmospheric drag, but TanDEM-X has the additional task of maintaining the desired formation via relative control maneuvers to correct for the natural drift of the formation. In more detail, in order to meet the relative control requirements of the 20 m crosstrack and 200 m alongtrack directions, TanDEM-X has to 1) compensate the natural deviation of the relative eccentricity vector, 2) counteract the natural drift of the inclination vector, 3) control the alongtrack separation that is perturbed by relative drag and in-plane maneuver execution errors, and 4) replicate the TerraSAR-X orbit-keeping maneuvers. The out-of-plane relative orbit maintenance and the larger absolute orbit maintenance maneuvers (steps 2 and 4, respectively) are performed with four 1 N hydrazine thrusters. For the in-plane formation control (steps 1 and 3, respectively), two exclusive pairs of 40 mN cold-gas thrusters are used.

The relative orbit maintenance maneuvers are computed on ground, except for the TanDEM-X Autonomous Formation Flying campaign performed in March 2011, where three maneuver pairs per day were autonomously planned and executed on board. A linearized model was used to describe the relative motion for formation design and relative control purposes. In further detail, the well-known Hill-Clohessy–Wiltshire (HCW) model is recast in terms of relative orbital elements (ROEs)[§] and upgraded to include J2 effects and impulsive delta-v maneuvers.

The formation design is based on the e/i vector separation concept. The key idea of this approach resides in the fact that the uncertainty in predicting the alongtrack separation of two spacecraft is generally much higher than the radial and crosstrack components. Moreover, because of the coupling between relative semimajor axis and relative argument of latitude, uncertainties affecting the initial position and velocity due, for instance, to orbit determination errors will result in a secular grow of the errors in alongtrack direction [22]. Then, the relative motion between spacecraft can only be considered safe in the presence of alongtrack uncertainties if a separation in radial and alongtrack directions is ensured at all times. This condition can be achieved by a parallel (or antiparallel) alignment of the relative eccentricity and inclination vectors (see Fig. 9 [31]).

In light of the aforementioned, the configuration of the formation is designed, based on the following requirements:

1) The relative semimajor axis has to be as small as possible ($\delta a^{\text{nom}} \approx 0$) to reduce the drift of the relative mean argument of latitude.

2) The modulus of the relative eccentricity vector has to be limited by the minimum necessary separation for safe operation and maximum alongtrack separation required for interferometry (200 m $< a\delta e <$ 50 m).

3) The modulus of the relative inclination vector follows the same constraints as used by the relative eccentricity vector (200 m $< a\delta i <$ 500 m).

4) The inclination difference has to be zero to avoid secular drift of the y component of the relative inclination vector δi_y due to J2 perturbation.

5) The relative inclination vector has to have a nominal phase angle of $\vartheta^{\text{nom}} = \pm\pi/2$.

6) The relative eccentricity vector has to be closely aligned to the relative inclination vector (i.e., $\varphi^{\text{nom}} = \pm\pi/2$) so as to ensure maximum crosstrack separation.

In conclusion, the nominal values of relative eccentricity and inclination vectors have to be [24]

$$\boldsymbol{\delta e}^{\text{nom}} = \begin{bmatrix} \delta e_x^{\text{nom}} \\ \delta e_y^{\text{nom}} \end{bmatrix} \approx \delta e^{\text{nom}} \begin{bmatrix} 0 \\ \pm 1 \end{bmatrix}$$
$$\boldsymbol{\delta i}^{\text{nom}} = \begin{bmatrix} \delta i_x^{\text{nom}} \\ \delta i_y^{\text{nom}} \end{bmatrix} \approx \delta i^{\text{nom}} \begin{bmatrix} 0 \\ \pm 1 \end{bmatrix} \tag{3}$$

To meet the aforementioned requirements, TanDEM-X performs a series of tangential double-impulse and perpendicular single-impulse maneuvers. The magnitudes of these impulses are computed using the simplified Gauss equations, adapted for the near-circular nonequatorial orbits [32], i.e.,

$$\Delta\delta\boldsymbol{\alpha} = \begin{bmatrix} \Delta\delta a \\ \Delta\delta\lambda \\ \Delta\delta e_x \\ \Delta\delta e_y \\ \Delta\delta i_x \\ \Delta\delta i_y \end{bmatrix} = -\frac{1}{n_d a_d} \begin{bmatrix} 0 & 2 & 0 \\ -2 & -3(u_d - u_M) & 0 \\ \sin(u_M) & 2\cos(u_M) & 0 \\ -\cos(u_M) & 2\sin(u_M) & 0 \\ 0 & 0 & \cos(u_M) \\ 0 & 0 & \sin(u_M) \end{bmatrix} \begin{bmatrix} v_r \\ v_t \\ v_n \end{bmatrix} \tag{4}$$

where n_d, a_d, and $u_d = M_d + \omega_d$ are the mean motion, the semimajor axis, and the mean argument of latitude of TanDEM-X orbit, with M_d as the mean anomaly and ω_d as the argument of perigee. Also, u_M denotes the mean argument of latitude at the maneuver time t_M. The vector $\Delta\delta\alpha$ corresponds to the variations of the relative orbital elements:

$$\delta\boldsymbol{\alpha} = \begin{bmatrix} \delta a \\ \delta\lambda \\ \delta e_x \\ \delta e_y \\ \delta i_x \\ \delta i_y \end{bmatrix} = \begin{bmatrix} \frac{a_d}{a_c} - 1 \\ u_d - u_c + \cos(i_c)(\Omega_d - \Omega_c) \\ e_d\cos(\omega_d) - e_c\cos(\omega_c) \\ e_d\sin(\omega_d) - e_t\sin(\omega_c) \\ i_d - i_c \\ \sin(i_c)(\Omega_d - \Omega_c) \end{bmatrix} \tag{5}$$

induced by the instantaneous velocity changes $[v_r, v_t, v_n]^T$ in the radial, alongtrack, and crosstrack directions. The subscripts "c" and "d" stand for the "chief" and "deputy," respectively, and therefore correspond to TerraSAR-X and TanDEM-X.

[§]We refer the reader to [38] and [32] for a comprehensive description of ROEs.

The aim of formation control is to maintain the actual orbital relative element $\delta\alpha_i$ in a symmetric control window centered on the nominal value $\delta\alpha_i^{\text{nom}}$, i.e., $|\delta\alpha_i - \delta\alpha_i^{\text{nom}}| \leq \delta\alpha_i^{\max}$. In other words, when the magnitude of the relative e/i vectors tracking errors $\|\delta\boldsymbol{e} - \delta\boldsymbol{e}^{\text{nom}}\|$ and $\|\delta\boldsymbol{i} - \delta\boldsymbol{i}^{\text{nom}}\|$ exceed the maximum admissible deviations $\delta e^{\max}$ and $\delta i^{\max}$ respectively, an in-plane maneuver or out-of-plane maneuver is performed. According to Eq. (4), the following set of tangential double-impulse maneuver and single-impulse maneuver is implemented to control the in-plane and out-of-plane relative motions, respectively [22,24,33]:

$$
\begin{aligned}
v_t^1 &= \frac{na}{4}[(\delta a^{\text{man}} - \delta a) + \|\delta\boldsymbol{e}^{\text{man}} - \delta\boldsymbol{e}\|] \\
u_{M1} &= \text{atan}((\delta e_y^{\text{man}} - \delta e_y)/(\delta e_x^{\text{man}} - \delta e_x)) \\
v_t^2 &= \frac{na}{4}[(\delta a^{\text{man}} - \delta a) - \|\delta\boldsymbol{e}^{\text{man}} - \delta\boldsymbol{e}\|] \\
u_{M2} &= u_{M1} - \pi
\end{aligned} \tag{6}
$$

$$
\begin{aligned}
v_n &= na\|\delta\boldsymbol{i}^{\text{man}} - \delta\boldsymbol{i}\| \\
u_M &= \text{atan}((\delta i_y^{\text{man}} - \delta i_y)/(\delta i_x^{\text{man}} - \delta i_x))
\end{aligned} \tag{7}
$$

In Eqs. (6) and (7), the terms δa^{man} and $\delta\boldsymbol{e}^{\text{man}}$ indicate the value of the relative semimajor axis and relative eccentricity vector, respectively, after the double-impulse in-plane maneuver; whereas and are the actual values right before the execution of the first impulse (see Fig. 10). Similarly, $\delta\boldsymbol{i}^{\text{man}}$ and $\delta\boldsymbol{i}$ represent the relative inclination vector after and before the crosstrack single-impulse maneuver, respectively (see Fig. 10).

The eccentricity vector after the application of the two impulses reported in Eq. (6), taking into account the natural drift of the relative eccentricity vector between the two impulses due to the J2 perturbation, is given by [24,32]

$$
\delta\boldsymbol{e}^{\text{man}} = \boldsymbol{R}(\delta\varphi^{\max})\delta\boldsymbol{e}^{\text{non}} = \boldsymbol{R}(\delta\varphi^{\max})\begin{bmatrix} \delta e_x^{\text{non}} \\ \delta e_y^{\text{non}} \end{bmatrix} \tag{8}
$$

with

$$
\begin{aligned}
\boldsymbol{R} &= \begin{bmatrix} \cos(\delta\varphi^{\max}) & -\sin(\delta\varphi^{\max}) \\ \sin(\delta\varphi^{\max}) & \cos(\delta\varphi^{\max}) \end{bmatrix} \\
\varphi^{\max} &= \text{sign}(\varphi')\arcsin\left(\frac{\delta e^{\max}}{\delta e^{\text{nom}}}\right) + \varphi'\Delta u_M \\
\varphi' &= \frac{3}{2}J_2\left(\frac{R_{\text{EARTH}}}{a}\right)^2(5\cos(i)^2 - 1) \\
\Delta u_M &= u_{M2} - u_{M1} = -\pi
\end{aligned} \tag{9}
$$

Similarly, the relative inclination vector desired after the execution of the out-of-plane maneuver is given by

$$
\delta\boldsymbol{i}^{\text{man}} = \begin{bmatrix} \delta i_x^{\text{nom}} \\ \delta i_y^{\text{nom}} - \text{sign}(\delta i_x)\delta i^{\max} \end{bmatrix} \tag{10}
$$

It is worth remarking that the maneuver times (u_{M1}, u_{M2}, and u_M) are determined through the design parameters δe_x^{nom}, δe_y^{nom}, δi_x^{nom}, δi_y^{nom}, $\delta e^{\max}$, and $\delta i^{\max}$ as follows:

$$
\begin{aligned}
\delta\boldsymbol{e}^t &= \boldsymbol{R}(-\delta\varphi^{\max})\delta\boldsymbol{e}^{\text{nom}} \\
u_{M1} &= \text{atan}\left(\frac{(\delta e_y^{\text{man}} - \delta e_y^t)}{(\delta e_y^{\text{man}} - \delta e_x^t)}\right) \qquad u_{M2} = u_{M1} - \pi \\
\delta\boldsymbol{i}^t &= \begin{bmatrix} \delta i_x^{\text{nom}} \\ \delta i_y^{\text{man}} - \text{sign}(\delta i_x)\delta i^{\max} \end{bmatrix} \\
u_M &= \text{atan}((\delta i_y^{\text{man}} - \delta i_y^t)/(\delta i_x^{\text{man}} - \delta i_x^t))
\end{aligned} \tag{11}
$$

In other words, the first alongtrack impulse and the crosstrack maneuver are located at a mean argument of latitude that matches the phase of the relative e/i-vector corrections (see Fig. 10). Note that the in-plane maneuver cycle ΔT [omitted] (i.e. the time interval comprised between the first pulses of the double-impulse maneuver) is set to an integer number of the TanDEM-X period.

3. Prototype Research Instruments and Space Mission Technology Advancement

Developed by the Swedish Space Corporation with contributions from the DLR, the French Space Agency Centre National d'Etudes Spatiales (CNES), and the Danish Technical University, Prototype Research Instruments and Space Mission technology Advancement is a formation-flying demonstration mission launched in June 2010. The two satellites were launched to a sun-synchronous near-circular dawn–dusk orbit ($i = 98.28$ deg, $e = 0.004$) with an initial mean altitude of 757 km. The formation consists of a main satellite (also named Mango, 150 kg) and a target satellite (also named Tango, 50 kg) [34]. The mission's primary objectives include testing and validation of GNC hardware, software, and algorithms for autonomous formation flying (separation distance: 5 km–20 m), homing and rendezvous (separation distance: 100 km–3 m), proximity operations (separation distance: 100–3 m), and final approach and recede operations (separation distance: 3–0 m) [35]. Specifically, the situations to be examined include autonomous formation flying based on a GPS system and a formation-flying radio-frequency (FFRF) sensor system, homing and rendezvous based on vision-based sensing (VBS), proximity operations based on GPS and VBS, and final approach and recede operations based on VBS [34]. The PRISMA satellites are equipped with two intersatellite links: one for telecommands and telemetry, and the other integrated into the RF-metrology sensor [35,36]. Each satellite

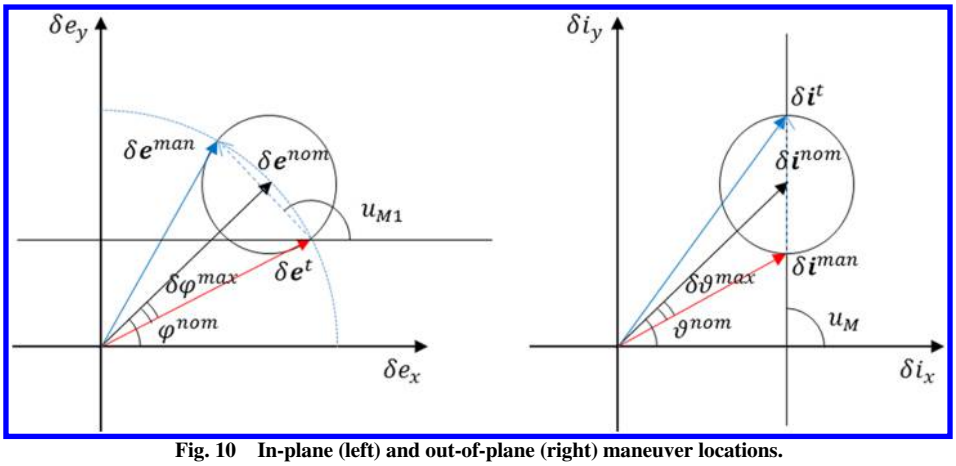

Fig. 10 In-plane (left) and out-of-plane (right) maneuver locations.

has two miniature Phoenix GPS receivers and the FFRF metrology system, which consists of one Rx/transmitter (Tx) master and two Rx slave antennas on the main spacecraft and three single Rx/Tx antennas on the target. The main spacecraft is additionally equipped with four camera heads: two used for far-range and short-range navigation, and two as star trackers (microASC vision sensor [34]). Infrared light-emitting diodes (LEDs) are mounted on the target spacecraft to aid the VBS system in cooperative mode [36]. Finally, the main satellite hosts three separate propulsion systems: 1) a hydrazine system with six 1 N thrusters (total ΔV of 110 m/s), 2) a high-performance green propellant experimental system with two 1 N thrusters (total V of 60 m/s), and 3) an experimental cold-gas microthruster system. Note that both the main and target satellites have attitude control capability. The main spacecraft uses a reaction-wheel-based attitude control system, whereas the target uses magnetorquer-based three-axis attitude control [36].

a. Navigation Solution. The primary relative navigation sensor of the PRISMA formation is a GPS-based navigation system developed by DLR/GSOC [19]. The relative GPS serves as both a safe mode sensor of the formation to support failure detection, isolation, and recovery tasks like collision avoidance, and as navigation source for the onboard feedback controllers to enable autonomous formation-flying and rendezvous experiments. The GPS-based navigation system consists of a hardware architecture based on Phoenix-S receivers [37], which is identical on board the two satellites and a navigation software embedded in the Mango onboard computer for real-time absolute and relative navigation. The required accuracies for absolute and relative orbit determination are and 0.1 m, respectively. An extended Kalman filter (EKF) is implemented to get the navigation solution, processing pseudorange and carrier phase measurement data issued by the local Phoenix GPS receiver on the main satellite and sent via an intersatellite link from the remote Phoenix GPS receiver on the target. More specifically, the filter uses a linear combination of pseudorange and carrier-phase data (known as GRAPHIC, which stands for group and phase ionospheric correction) to estimate the absolute orbit and single difference carrier phase measurements to determine the relative orbit. Thus, the accuracy of the relative navigation is driven by the single-difference carrier phase measurements, whereas the absolute navigation accuracy is driven by the noise of the GRAPHIC measurements. Note that the relative spacecraft state is simply computed by differencing the absolute states without the need of an explicit relative motion model. The absolute orbit model for each spacecraft includes gravitational and nongravitational forces. More specifically, the GRACE GRACE Gravity Model 01S gravity field up to the order and degree of 15 is adopted to obtain the acceleration due to the Earth's static gravity field; in addition, accelerations due to solar radiation pressure and atmospheric drag are taken into account. Finally, empirical accelerations in the radial, alongtrack, and crosstrack directions are modeled as a first-order Gauss–Markov process and estimated by the reduced-dynamic Kalman filter to compensate for modeling deficiencies in the employed dynamic models [37].

Two experiments carried out during the PRISMA mission are mentioned here: the Advanced Rendezvous demonstration using GPS and Optical Navigation (ARGON) experiment, and the Formation Flying In-Orbit Ranging Demonstration (FFIORD), conceived and designed by the German Space Operations Center of the DLR and CNES, respectively.

The ARGON experiment aimed primarily at demonstrating a man-in-the-loop far-range rendezvous to a noncooperative, passive, and unknown client using vision-based navigation. The optical navigation system embarked on the main satellite was based on a fully autonomous miniature star sensor (microASC) platform consisting of two camera head units named VBS FAR and VBS CLOSE (see [33] for more details on the VBS system). During ARGON experiment execution, VBS FAR was used exclusively for angles-only navigation and only for imaging purposes. To obtain the relative navigation solution through the line-of-sight vectors provided by the image-processing module, an iterative dynamics batch least-squares estimator with a priori information was implemented based on the linear ROE-based dynamical model including the J2 effect [38].

The main goals of the FFIORD experiment were to perform a flight validation of the FFRF subsystem and test the algorithms for maintenance of close formation using data from the FFRF. The FFRF instrument can offer relative positioning for up to four satellites flying in formation, providing an intersatellite distance with an accuracy of 1 cm, an azimuth and elevation of the line of site (LOS) between the spacecraft with an accuracy of 1 deg, and the time bias between the satellite clocks (more details on the FFRF can be found in [19,39]). During the FFIORD experiment, an EKF was exploited to obtain the relative position and velocity. Different relative dynamical models are used for the implementation of the navigation filter, such as the HCW, the Yamanaka–Ankersen (YA), and the Tshauner–Hempel including the differential acceleration due to J2 [39].

b. Formation Control and Guidance Solutions. Different approaches are used to control the relative orbit of the main satellite with respect to the target satellite, depending on the executed experiments during the mission. Hereafter, a brief description of algorithms implemented for relative motion control in the correspondence of each experiment is reported. For a more comprehensive review of the GNC modes, we address the reader to [19] (chapter 21).

In the Autonomous Formation Flying (AFF) and Proximity Operations/Final Approach and Recede Maneuvers (PROX/FARM) experiment, the model predictive control (MPC) framework is used for relative orbit control; more specifically, the Yamanaka–Ankersen state transition matrix is used to propagate the orbit within the MPC optimization step. Note that, even though the same control framework is used for the AFF and PROX/FARM modes, different settings for the propagation horizon and actuation frequency are implemented. Furthermore, let us point out that a different set of sensors is exploited in the aforementioned experiments. Although the AFF aims at demonstrating GPS-based passive formation flying, PROX/FARM modes include close-range forced-motion operation based on the GPS or VBS navigation data (see Table 2).

The DLR mode is operative during the Spaceborne Autonomous Formation Flying Experiment (SAFE) and the Autonomous Orbit Keeping (AOK) experiment [19]. SAFE is intended to test a guidance law for a safe collision-free separation strategy and a robust control algorithm for formation keeping and reconfiguration with an accuracy better than 30 m for a separation below 1 km [40]. On the other hand, the AOK experiment is designed to demonstrate the capability of a spacecraft to autonomously control the osculating longitude of the ascending node (i.e., absolute control of the spacecraft) with an accuracy of 10 m. Both of the aforementioned experiments adopt an analytical feedback control algorithm, taking advantage of a convenient parameterization of the relative motion based on ROEs [41,42].

The CNES mode is used when the FFIORD experiment is carried out. During this experiment, different FF operations are performed, such as autonomous rendezvous, station keeping at different distances and offset positions from the orbit track, low-speed translations in plane and out of plane, and collision-avoidance maneuvering. Different orbit control functions are implemented. For rendezvous purposes, impulsive maneuvers determined by inverting the Yamanaka–Ankersen state transition matrix are performed.

Table 2 Summary of orbit control techniques and navigation sensors used PRISMA mission [19]

GNC modes	Navigation sensors	Relative orbit control
AFF	GPS	MPC
Manual mode	— —	Impulsive
DLR	GPS	Impulsive feedback control
CNES	FFRF	Impulsive maneuver, LQR, MPC
ARV (autonomous rendezvous)	VBS	Impulsive feedback control, MPC
PROX	GPS or VBS	MPC
FARM	VBS	MPC

In contrast, a linear quadratic control is designed for the proximity operations. Finally, a MPC-like method with fixed maneuver dates and L2-norm criteria for the minimization of the propellant consumption is designed for safe rendezvous or deployment from a distance of about 10 to 100 m [19].

Depending on the operating GNC mode, different guidance laws are implemented. The AFF mode uses passive target orbits uplinked from the ground. During the PROX/FARM experiment, the guidance function computes the optimal path among a set of nodes (flight map) through optimization algorithms based on the solutions of linear and integer programming problems. Finally, when the DLR mode is operative, the onboard guidance system uses eccentricity/inclination vector separation to avoid collision hazards from alongtrack position uncertainties through the proper separation of the two spacecraft in radial and crosstrack directions [35]. This approach guarantees maximum operational safety in contingency cases and proves robustness under the presence of maneuver execution errors as well as communication losses.

4. *Canadian Advanced Nanosatellite eXperiment-4 and -5*

The Canadian Advanced Nanosatellite eXperiment-4 and -5 mission, developed by the Space Flight Laboratory at the University of Toronto Institute for Aerospace Studies, is a dual-satellite formation-flying demonstration launched in June 2014 [43]. The primary objective of the pair of nanosatellites (each 20 cm cube weighing approximately 6 kg [44]) is to demonstrate formation flying with a position control error of less than 1 m and a relative position estimation error of less than 10 cm with low ΔV. The two spacecraft were placed in a sun-synchronous near-circular orbit ($i = 98.2$ deg, $e = 0.001$) at the initial mean altitude of 650 km. The mission covers four separate formations: 1000 m alongtrack orbit (ATO), 500 m ATO, 100 m projected circular orbit (PCO), and 50 m PCO, where ATO indicates that a fixed distance is kept between the two satellites in the same orbital plane in a "leader–follower" configuration and PCO indicates that one satellite appears to orbit around the other while traversing an orbit [44]. CanX-4 and CanX-5 are both based on the generic nanosatellite bus [43]. CanX-4 is designated the role of chief, whereas CanX-5 is deputy. Each satellite is equipped with an S-band transmitter and two S-band patch antennas for downlink, as well as an ultrahigh-frequency receiver with a canted turnstile antenna system for uplink. Data are passed between the satellites via an S-band intersatellite link [44]. Both satellites have the Canadian Nanospace Propulsion System for orbit acquisition and phasing, station keeping, and formation control and reconfiguration, consisting of four independently controlled cold-gas thrusters arranged on one side of the satellite [45] and providing an approximated total ΔV of 18 m/s [44].

a. Navigation Solution. The three pieces of navigation and control software used to meet the formation control requirements are the formation-flying integrated onboard nanosatellite algorithm (FIONA), the relative navigation (RelNav) algorithm, and the onboard attitude system software (OASYS). The OASYS runs on both spacecraft, whereas FIONA and RelNav run only on the deputy. The FIONA computes formation-keeping and reconfiguration control maneuvers, and it performs absolute state estimation of both satellite orbits. It is responsible for autonomously computing the formation reconfiguration and formation-keeping control maneuvers. The FIONA implements an extended Kalman filter to estimate the absolute states of both the chief and deputy spacecraft later used to compute the auxiliary control parameters and map the relative state estimated by RelNav into the local vertical local horizontal frame [44].

The RelNav algorithm is an extended Kalman filter that uses carrier phase differential GPS techniques to estimate the relative state of the deputy with respect to the chief [44]. Single-difference pseudorange and carrier phase measurements were selected over double differences for computational efficiency and an increased chance of filter convergence [45]. The state vector used by RelNav is given as $\boldsymbol{x} = [\Delta \boldsymbol{r}^T, \Delta \dot{\boldsymbol{r}}^T, \Delta b, \Delta N_1, \ldots, \Delta N_m]^T$, where $\Delta \boldsymbol{r}$ is the relative position expressed in the Earth-centered Earth-fixed reference frame, $\Delta \dot{\boldsymbol{r}}$ is the relative velocity, Δb is the differential clock error, and ΔN_i is the ith floating point single-difference carrier phase ambiguity [44].

The relative state is propagated using pseudorelative dynamics [44]. Given a chief position $R_{c,k}$ and velocity $\dot{R}_{c,k}$ at time t_k, the deputy position and velocity at time t_k are given by $R_{d,k} = R_{c,k} + \Delta r_k$ and $\dot{R}_{d,k} = \dot{R}_{c,k} + \Delta \dot{r}_k$. The relative state at time t_{k+1} is obtained by integrating the perturbed absolute equations of motion using one step of a fourth-order Runge–Kutta method for the chief and deputy, and finally subtracting to obtain the relative states $\Delta r_{k+1} = R_{d,k+1} - R_{c,k+1}$ and $\Delta \dot{r}_{k+1} = \dot{R}_{d,k+1} - \dot{R}_{c,k+1}$ [45]. The measurements are assumed to be uncorrelated, allowing the use of scalar measurement updates, which reduces computational cost [44].

b. Formation Control and Guidance Solutions. The CanX-4&5 mission uses a control system called the drift recovery and station-keeping (DRASTK) system to bring the deputy and chief spacecraft into close proximity after ejection from the launch vehicle, placing one spacecraft directly behind the other (approximately 3 km apart) with as close to zero relative motion as possible. It aims to match all orbital elements between the two satellites except true anomaly, which is allotted a small difference. The control scheme implemented for this task is based on Gauss variational equations. DRASTK accounts for fuel spent on maneuvers, propellant leakage over time, and the desire to maximize the number of thrusts that take place in sunlight, where attitude control is more reliable [44].

Once positioned in close proximity, the CanX-4&5 mission uses the FIONA system, which consists of two types of controllers: one each for formation keeping and reconfiguration. The FIONA regularly determines the tracking error of the chaser and computes the optimal thrusts to correct the error, implementing a pulsewidth modulation strategy [46].

The FIONA's formation-keeping controller is a discrete linear quadratic regulator (LQR) designed using the tracking error $\tilde{\boldsymbol{x}} = \boldsymbol{x} - \boldsymbol{x}_{\text{ref}}$ as a controller state. The reference trajectories $\boldsymbol{x}_{\text{ref}}$ are the periodic solutions to the HCW equations, i.e.,

$$\begin{aligned} x(t) &= \frac{1}{2} d_1 \sin(nt + \alpha) \\ y(t) &= d_1 \cos(nt + \alpha) + d_3 \\ z(t) &= d_2 \sin(nt + \beta) \end{aligned} \tag{12}$$

where n is the mean orbital motion of the chief satellite; and d_1, d_2, d_3, α, and β are the formation design parameters and depend on the formation configuration, i.e., ATO or PCO (see Table 3).

The FIONA's formation reconfiguration controller algorithm identifies a set of impulsive maneuvers that minimize an energylike cost function such that the final desired state is reached in the desired amount of time. The reconfiguration algorithm requires a start time and end time, as well as the number of impulses, and it uses the Yamanaka–Ankersen state transition matrix (STM) to determine the final state. Hereafter, the YA STM is reported for completeness:

$$\boldsymbol{x}(t) = [x, \dot{x}, y, \dot{y}, z, \dot{z}]^T = \phi(f)\phi^{-1}(f(0))\boldsymbol{x}(t_0) \tag{13}$$

with

Table 3 Formation design parameters [44]

Formation configuration	d_1, m	d_2, m	d_3, m	α, rad	β, rad	Duration, orbits
ATO 1000	60	30	1000	0	$\pi/2$	11
ATO 500	60	30	500	0	$\pi/2$	11
PCO 1000	100	100	0	0	0	11
PCO 50	50	50	0	$(3/2)\pi$	$(3/2)\pi$	11

$$\phi(f) = \begin{bmatrix} s & c & 2-3esI & 0 & 0 & 0 \\ \dot{s} & \dot{c} & -3e\left(\dot{s}I + \frac{s}{k^2}\right) & 0 & 0 & 0 \\ c\left(1+\frac{1}{k}\right) & -s\left(1+\frac{1}{k}\right) & -3k^2 I & 1 & 0 & 0 \\ -2s & e-2c & -3(1-2esI) & 0 & 0 & 0 \\ 0 & 0 & 0 & 0 & \cos f & \sin f \\ 0 & 0 & 0 & 0 & -\sin f & \cos f \end{bmatrix}$$

$$\phi^{-1}(f_0) = \frac{1}{\eta^2}\begin{bmatrix} -\frac{3s(k+e^2)}{k^2} & c-2e & 0 & -\frac{s(k+1)}{k} & 0 & 0 \\ -3\left(e+\frac{c}{k}\right) & -s & 0 & -\left(\frac{c(k+1)}{k}+e\right) & 0 & 0 \\ 3k-\eta^2 & es & 0 & k^2 & 0 & 0 \\ -\frac{3es(k+1)}{k^2} & -2+ec & \eta^2 & -\frac{es(k+1)}{k} & 0 & 0 \\ 0 & 0 & 0 & 0 & \eta^2\cos f & -\eta^2\sin f \\ 0 & 0 & 0 & 0 & \eta^2\sin f & \eta^2\cos f \end{bmatrix} \tag{14}$$

where $s = k\sin f$, $c = k\cos f$, $k = 1 + e\cos f$, $I = (\mu^2/h^3)(t - t_0)$, and $\eta = \sqrt{1-e^3}$, with h as the orbital angular momentum of the chief and f as the true anomaly [7]. The Yamanaka–Ankersen STM is chosen for its fidelity and computational efficiency. The thrusts are spaced equally through the time domain specified by defined start and end times [44].

5. *Magnetospheric Multiscale*

The Magnetospheric Multiscale mission is a tetrahedral formation made of four spacecraft operating in high elliptical orbits (1.2 Earth radii perigee and 12 Earth radii apogee radius), developed by NASA and launched in March 2015. The mission's primary objective is to study magnetic reconnection, energetic particle acceleration, and turbulence in the Earth's magnetosphere. The mission includes the following two phases [47]:

1) In phase 1, the data are collected for the "day side" of the magnetic field while the tetrahedral formation is resized from 160 to 10 km on a highly elliptical orbit.

2) In phase 2, first, a series of maneuvers are executed to incrementally increase the orbital apogee of each spacecraft from 12 Earth radii to 25 Earth radii. Then, data are collected for the "night side" of the magnetic field while the formation is resized from 400 to 30 km.

The main challenge of the mission is to maintain a sufficient safe distance between satellites while keeping close enough formation to enable significant data collection and performing as few maneuvers as possible. The satellites are identical and have a launch mass of 1354 kg, except for satellite 4 placed at the top of launch stack that is lighter (launch mass of 1339 kg) [48]. Each MMS satellite in the formation is equipped with 12 monopropellant thrusters (eight 17.8 N thrusters oriented radially, and four 4.4N thrusters oriented axially), which are capable of modulating the command signal through the pulsewidth modulation technique. Moreover, each observatory is equipped with a microASC star tracker system (STS), two digital sun sensors (DSSs), an acceleration measurement system (AMS), and a GPS navigation system extremely sensitive to provide absolute position information at the mission high altitude. The STS and AMS are the primary closed-loop feedback sensors for attitude and translational control, respectively. The STS provides time-stamped attitude quaternion data packets at 4 Hz with a 3σ transverse and boresight axis accuracies of 60 and 200 arcsec onds, respectively. The AMS provides three-axis acceleration measurements and integrates these samples in order to get the spacecraft velocity change. It has a dynamic range of $\pm 25{,}000$ μg, a resolution of 1 μg, and an effective bandwidth of 250 Hz. The DSS provide the sun elevation in order to time thruster pulses to get a power-positive and thermally safe spacecraft orientation (sun acquisition mode) [48,49].

a. Navigation Solution. To perform the high-accuracy orbit determination required for the formation maintenance, an onboard navigation system is exploited. It consists of four GPS receivers, an ultrastable oscillator, a signal processor card (SPC), and a RF card. All the aforementioned hardware are duplicated for redundancy. The navigation requirements depend on the operative conditions. During the science phases, the absolute orbital positions of the spacecraft have to be known to be within 100 km, root sum squares; whereas the separation distance between the spacecraft has to be known to within the greater of 1% or 100 m. In addition, the onboard orbit determination system has to provide absolute and relative orbit solutions with a mean semimajor axis accuracy of 50 and 70 m, respectively, for regions above three Earth radius [50]. The navigation system uses GPS L1 pseudorange measurements and processes them through the Goddard Enhanced Onboard Navigation System (GEONS) software installed on the SPC. The GEONS software uses an extended Kalman filter to estimate the spacecraft's position, velocity, clock bias with respect to GPS time, clock bias rate, and clock bias acceleration. The GEONS implements a high-fidelity dynamical model including the effects of Earth oblateness, atmospheric drag, solar radiation pressure, and the gravity of near bodies. High-resolution thrust acceleration measurements from the onboard accelerometer are also included in the filter to model the formation maintenance maneuvers [50]. Table 4 summarizes the GEONS configuration.

b. Formation Control and Guidance Solutions. To accurately control the geometry of formation, a closed-loop controller is implemented on the attitude control subsystem (ACS) software. The MMS controller is able to control all six degrees of freedom (6DOFs) using

Table 4 GEONS software configuration

GEONS software elements	Features
Estimator	Extended Kalman filter EKF. Estimation frequency of 30 s for maximum 12-GPS pseudorange measurements Fourth-order Runge–Kutta
Dynamical model	Earth gravity model: 13×13 joint earth gravity models-2 Atmospheric drag: Harris–Priester atmospheric density model Solar radiation pressure: Spherical area model Solar/lunar ephemeris: Polynomial fit to JPL definitive ephemeris (DE)404 Maneuver model: Finite burn using 10 s averaged accelerations

separate logic for velocity control (translational motion, Delta-V mode) and momentum control (rotational motion, Delta-H mode). The velocity controller is a classic tracker with both a time-varying target and velocity-estimate feedback. A predetermined velocity change profile $\Delta \boldsymbol{v}_{\text{target}}$ is uploaded to the spacecraft before each maneuver in the form of a piecewise linear lookup table (velocity in ECIJ2000 versus spacecraft time) [49]. The velocity change estimate is defined as the expected value of the true variation value, i.e.,

$$\Delta \hat{\boldsymbol{v}} = E(\Delta \boldsymbol{v}_{\text{true}}) \tag{15}$$

where $\Delta \boldsymbol{v}_{\text{true}}$ is computed by [51]

$$\Delta \boldsymbol{v}_{\text{true}} = \int_{t_1}^{t_2} \boldsymbol{S}_b^i \boldsymbol{a}_k^{(b)}\,\mathrm{d}\tau + \left[\boldsymbol{S}_b^i \boldsymbol{\omega}^{(b)} \times \boldsymbol{r}_{cd}^{(b)} - \boldsymbol{S}_b^i \dot{\boldsymbol{r}}_c^{(b)}\right]_{t_1}^{t_2} - \int_{t_1}^{t_2} \boldsymbol{S}_b^i \boldsymbol{b}^{(b)}\,\mathrm{d}\tau - \int_{t_1}^{t_2} \boldsymbol{S}_b^i \boldsymbol{\eta}^{(b)}\,\mathrm{d}\tau \tag{16}$$

The symbol $\boldsymbol{S}_b^i$ in Eq. (16) indicates the direction-cosine matrix transformation from the body fixed to the inertial reference frame. Note that $\boldsymbol{a}_k^{(b)}$ is the sampled acceleration provided by the accelerometer in the AMS, $\boldsymbol{\omega}^b$ is the spacecraft angular velocity, $\boldsymbol{r}_{cd}^{(b)}$ is the position vector from the spacecraft center of mass to the accelerometer head, and $\boldsymbol{r}_c^b$ is the position of the spacecraft center of mass. The terms $\boldsymbol{b}^{(b)}$ and $\boldsymbol{\eta}^{(b)}$ are the electromechanical bias vector and sensor noise vectors, respectively. All vectors in Eq. (16) are expressed in the body reference frame. Let us recall that the measurements integral in Eq. (16),

$$\int_{t_1}^{t_2} \boldsymbol{S}_b^i \boldsymbol{a}_k^{(b)}\,\mathrm{d}\tau$$

are obtained by sampling the analog accelerometer of the AMS at 1 kHz. Because the velocity controller operates with a frequency of 4 Hz, the measurement integral contains 250 subsamples that are combined to generate a single velocity increment. Thus, before computing the integral, the ACS flight software transforms the kth sample forward in time to what is assumed will be the final reference frame, i.e.,

$$\int_{t_1}^{t_2} \boldsymbol{S}_b^i \boldsymbol{a}_k^{(b)}\,\mathrm{d}\tau \approx \boldsymbol{S}_{b_{250}}^i \sum_{k=1}^{250} \boldsymbol{S}_{b_k}^{b_{250}} \boldsymbol{a}_k^{(b_k)} \cdot (t_k - t_{k-1}) \tag{17}$$

where the attitude matrix superscript and subscript, "b_{250}" and "b_k," indicate the body orientation at times t_{250} and t_k, respectively. Finally, the velocity control regulates the servo-error quantity $\boldsymbol{e} = \Delta \boldsymbol{v}_{\text{target}} - \Delta \hat{\boldsymbol{v}}$.

The previously described velocity controller allows tracking the inertially commanded velocity profile with a maximum magnitude error of 5 mm/s (3σ) for maneuvers lower than 0.5 m/s and accuracy lower than 1% otherwise, as well as direction accuracy of 1.5 deg (see Table 5), in accordance with the formation maintenance maneuver execution requirements derived by the operational constraints of maneuvering the fleet no more often than once every week.

The MMS controller can also control the nutation, spin rate, and momentum slews (momentum control). This is based on the globally stable Lyapunov method and adapted for discrete thrusting use on the MMS. A detailed description of the momentum control law is out of the scope of this paper. However, a comprehensive analysis of the attitude controller can be found in [52].

Table 5 Maneuver required accuracy [51]

	Features	
Maneuver size	Magnitude	Direction
0–0.10	5 mm/s	40 → 5 deg
0.10–0.5	5 mm/s	5 → 1.5 deg
>0.5	1%	1.5 deg

6. Autonomous Vision Approach Navigation and Target Identification

Autonomous Vision Approach Navigation and Target Identification experiment is a secondary experiment within the DLR Firebird mission launched on 22 June 2016 with the purpose of demonstrating and testing systems for the safe fuel-efficient fully autonomous approach and rendezvous for on-orbit servicing of a noncooperative client satellite. The two satellites that make up the formation are the chaser BIROS (130 kg) and the target Berlin Experimental and Educational Satellite 4 (BEESAT-4; 1 Unit CubeSat, 1 kg) [53]. The BIROS satellite moves on a sun-synchronous orbit ($i = 97.56$ deg) at an altitude of 515 km. The system operates at far- to midrange alongtrack separation distances (10 km to hundreds of meters) [54]. BIROS is equipped with two GPS antennas and a single-direction propulsion system consisting of cold-gas (nitrogen, N_2) thrusters. An attitude control system slews maneuver the satellite body in the desired thrust direction. In addition, it carries a star tracker camera, which it uses for far-range imaging of the target [55]. The BEESAT-4 picosatellite has no orbital control.

a. Navigation Solution. AVANTI uses vision-based navigation, imaging the noncooperative "client" satellite using star tracker cameras. The navigation system uses a kinematic approach to identify the target satellite and the density-based spatial clustering of applications with noise (DBSCAN) algorithm to isolate spots on images, indicating the target satellite's trajectory. Luminosity information is used only when several bright spots are present as possible targets. The line-of-sight measurements are sent to an extended Kalman filter. The system uses ROE to characterize the relative state, using a linear dynamics model, subject to secular J2 perturbation effects and differential drag [53,56]. Including perturbations has been shown to improve observability of the dynamics system in the absence of range/depth information, motivating further research into developing analytical dynamics models that capture additional relevant perturbations [55].

b. Formation Control and Guidance. The maneuver planning (MAP) and commanding module included in the AVANTI software solves an optimal control problem over an extended period of time to determine multi-impulsive maneuvers required for formation reconfiguration and keeping, which minimize fuel consumption [55,57]. In further details, the optimization problem is split into two phases. First, the sequence of m relative orbital element states $\delta\boldsymbol{\alpha}_i$ to achieve the desired final state $\delta\boldsymbol{\alpha}_F$ is computed (guidance step). The search of intermediate configurations $\delta\boldsymbol{\alpha}_i$ is carried out by minimizing the delta-V cost expressed through the following objective function [57]:

$$J = \sum_{i=1}^{m} (\Delta\|\delta \boldsymbol{i}\|)_i^2 + \sum_{i=1}^{m} (\Delta\delta a)_i^2 + \sum_{i=1}^{m} (\Delta\delta\lambda)_i^2 + \sum_{i=1}^{m} (\Delta\|\delta \boldsymbol{e}\|)_i^2 \tag{18}$$

where $(\Delta\delta\boldsymbol{\alpha})_i$ indicates the ith variation of ROE [see Eq. (5)] occurring at time t_i. The final relative state is computed using the state transition matrix associated with the linear ROE-based dynamics model including the mean effect due to J2 and the differential drag. More specifically, the perturbing effect due to the atmospheric drag is included in the linear model of the relative dynamics as a linear variation of the relative semimajor axis with respect to the elapsed time, i.e.,

$$\delta\dot{a} = -\frac{1}{n} \Delta B \rho v^2 \tag{19}$$

where ΔB is the difference of the ballistic coefficients of the satellites; whereas ρ, ΔB, and n are the atmospheric density, the deputy (BIROS) velocity with respect to the atmosphere, and the mean motion.

The evolution $\boldsymbol{P}_0 = a\zeta_0 \rightarrow \boldsymbol{P}_F = a\zeta_F$, with

$$\zeta = \left[\delta\dot{a}, \delta a, \delta\lambda, \delta e_x, \delta e_y, \delta i_x, \delta i_y\right]^T$$

is determined through the following expression,

$$\boldsymbol{P}_F = \boldsymbol{\Phi}_{F,0}\boldsymbol{P}_0 + \boldsymbol{\Phi}_{F,1}a(\Delta\delta\boldsymbol{\alpha})_1 + \cdots + \boldsymbol{\Phi}_{F,m}a(\Delta\delta\boldsymbol{\alpha})_m \tag{20}$$

where $(\Delta\delta\boldsymbol{\alpha})_i$ represents the variations of ROEs that occur at time t_i due to the impulsive maneuver execution; and $\boldsymbol{\Phi}_{F,i}$ is

$$\boldsymbol{\Phi}_{F,i} = \begin{bmatrix} 1 & 0 & 0 & 0 & 0 & 0 & 0 \\ t_F - t_i & 1 & 0 & 0 & 0 & 0 & 0 \\ -\frac{3}{4}n\Delta t_i^2 & -\frac{3}{4}n\Delta t_i & 1 & 0 & 0 & -\frac{21}{2}n\gamma\sin(2i)\Delta t_i & 0 \\ 0 & 0 & 0 & 1 & -\dot{\varphi}\Delta t_i & 0 & 0 \\ 0 & 0 & 0 & \dot{\varphi}\Delta t_i & 1 & 0 & 0 \\ 0 & 0 & 0 & 0 & 0 & 1 & 0 \\ 0 & 0 & 0 & 0 & 0 & 3n\gamma\sin(i)^2\Delta t_i & 1 \end{bmatrix}$$

$$\Delta t_i = (t_F - t_i) \tag{21}$$

In Eq. (21), the terms γ and $\dot{\varphi}$ are $\gamma = J_2 R_{\text{EARTH}}^2/(2a^2(1-e^2)^2)$ and $\dot{\varphi} = 3/2n\gamma(5\cos(i)^2 - 1)$, respectively. The problem of minimizing the function J in Eq. (18) while satisfying the final condition reported in Eq. (20) consists of two disjointed problems in the subsets $(\Delta\delta\dot{a}, \Delta\delta a, \Delta\delta\lambda, \Delta\delta i_x, \Delta\delta i_y)$ and $(\Delta\delta e_x, \Delta\delta e_y)$ that can be solved analytically. The solution is omitted here for brevity. However, we address the reader to [57] for more details.

In the second phase, the magnitude and the locations of the maneuvers required to achieve the precomputed ROE discontinuities are scheduled in the permissible time slots by exploiting a fully analytical four-burn maneuvering scheme (i.e., three in-plane and one out-of-plane maneuvers) that locally guarantees the delta-V minimization [58]. The previously described solution implemented in the MAP allows definition of a passively safe trajectory during the whole reconfiguration period if a passively safe final state is reached from an initial one with similar eccentricity/inclination separation.

Ultimately, in order to reduce the collision risk between the satellites, the reconfiguration maneuver design is based on the e/i vector separation concept. A further tool for maneuver safety assessment is provided by a dedicated onboard unit, named onboard safety monitoring, which propagates the relative orbit through the analytical solution given by Eq. (20), starting from the latest ground-based best available true value of the relative state, in order to validate safety level of the postmaneuver trajectory.

A tabular summary of the previously presented missions is reported in the Appendix in Table A2.

III. GNC System Design

The onboard GNC system is responsible of the following tasks (see Fig. 11):

1) The first task is navigation. It has to determine/predict the state with the required accuracy to be provided the controller and the guidance functions. A navigation system generally consists of a filter that processes the various information inputs obtained from different sensors from the actuators or from external sources in the case of a communication link with the ground station. The purpose of such a filter is to obtain an estimate of the translational state with reduced noise errors.

2) The second task is guidance. It has to provide the desired state vector at each point in time, which will then be compared with the estimated state, provided by the navigation system, enabling the controller to generate the required commands. Thus, the guidance function has to a) determine the execution time and duration of maneuvers, and b) generate relative position and velocity profiles for closed-loop controlled trajectories and hold points.

3) The third task if control. It has to provide force commands to correct the deviations between guidance and navigation states. The performance of such a control loop is determined by the dynamic behavior and errors of its elements and by the disturbances acting on them.

As illustrated in Fig. 11, the control loops for trajectory control include the sensors for position/attitude measurements; the GNC functions, which are implemented in software in the onboard computer (i.e., the navigation, guidance, and control functions); and the thrusters and other actuators for position/attitude control.

In the following sections, we discuss the GNC performance requirements for each objective-related class of FF missions based on the survey presented in Sec. II. Let us remark that these requirements depend on many factors. First, they are derived from the mission objective. For the sake of the example, a synthetic-aperture radar (SAR)-interferometry mission such as TanDEM-X (see Sec. II.C.2) requires a relatively low relative orbit control accuracy (~200 m in the alongtrack direction) and a meter-level accuracy for the navigation accuracy. On the contrary, a dual-spacecraft telescope in LPO might need more stringent constraints on control and relative state determination accuracies to guarantee the functionality of the payload. In addition, the requirements of the GNC system depend on the level of autonomy of the spacecraft. For a complete autonomous system, GNC might perform FDIR operations, generally implemented by the control center on the ground.

A. Control Accuracy Requirements

In this section, we present the control accuracy requirements based on the survey presented in Sec. II for each objective-related class of FF missions, i.e., space science, Earth observation/remote sensing, and Earth science.

According to the authors of [13,59], the controller performance can be related to the mean intersatellite distance. More specifically, the achievable relative position accuracy has to be roughly two orders of magnitude lower than the intersatellite distance, if no other

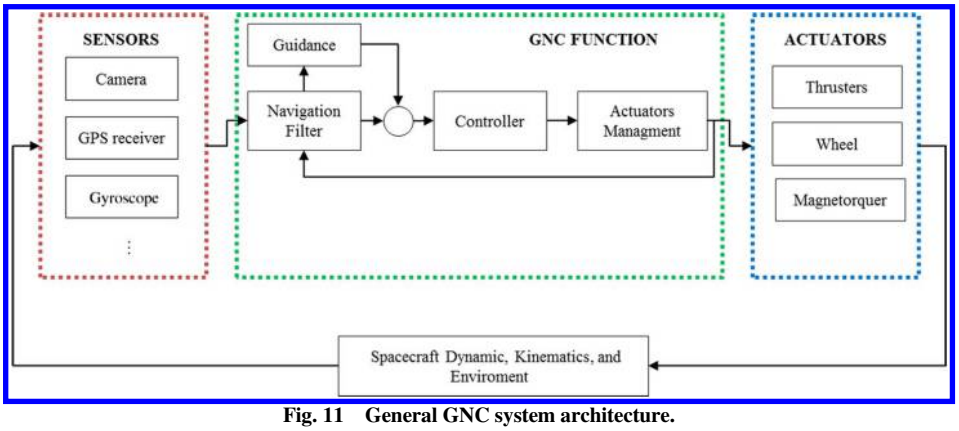

Fig. 11 General GNC system architecture.

Table 6 Relative orbit control accuracy and mean inter-satellite distance for objective-related class of FF missions

FF mission classes	Accuracy range	Intersatellite distance
Space science	0.1–10 cm	35 m–80,000 km
Earth science	100 m–50 km	50–200 km
Earth observation/remote sensing	10–200 m	50 m–100 km

requirements are imposed by the primary mission goal. Table 6 reports the typical performances required by a controller to execute the proximity operations. Space science missions tend to be the most demanding in terms of relative orbit control accuracy. These missions include, among others, space-based telescopes such as the X-ray evolving universe spectroscopy (XEUS) mission and a dual-spacecraft x-ray telescope operating in a low perturbed environment (e.g., LPO) and designed by the ESA in collaboration with NASA to investigate the high-redshift universe [60]; for this type of mission, high accuracy (order of millimeters to centimeters) is due to the alignment requirements for the observatory elements, the mirror, and the detector. A lower accuracy is generally needed by Earth observation/remote sensing and Earth science missions (hundreds of meters and kilometers, respectively). Two examples of these categories are TanDEM-X and GRACE. TanDEM-X requires a control accuracy of 20 m in the radial and normal direction and 200 m alongtrack, whereas the two spacecraft of GRACE have to maintain a relative alongtrack distance of 200 ± 50 km during the nominal science operations (see Secs. II.B and II.A, respectively, for more details).

Note that achieving the performances reported in Table 6 might pose different challenges from a control design standpoint, depending on the operating orbital regime. In other words, meeting high control accuracy in LEO (e.g., centimeter level) might be much more challenging than meeting the same requirement at the Lagrange point due to the different values of differential perturbing accelerations acting on the spacecraft.

B. Navigation Accuracy Requirements

This section shows the accuracy requirements for a navigation system based on the survey presented in Sec. II. Table 7 summarizes the relative position accuracy for each objective-related class of missions. Accordingly, the most demanding requirements are associated with space science missions. Let us remark that the low corresponding accuracy value reported in Table 7 relies on the deep-space dual-spacecraft telescope planned to fly in the future, as EXO-S or Stellar Imager. Future distributed systems for the deep-space observation, in fact, will require a high control performance to achieve their mission goals and, consequently, a navigation system that enables us to estimate the relative state with extraordinary precision. Earth science and Earth observation missions show less strict constraints on the navigation accuracy, varying from 1 to 10 m. This fact is due to the lower accuracy for these missions on the required control performances, as shown by Tandem-X and GRACE missions (see fourth columns in the Appendix in Table A2).

C. Overview of Relative Navigation Technology

At the present, five families of systems are used for the relative navigation in FF missions, i.e., 1) GPS-based systems, 2) RF-based systems, 3) radar systems, 4) vision-based systems, and 5) laser-based systems.

Table 7 Relative navigation accuracy for objective-related class of FF missions

FF mission classes	Accuracy range
Space science	1 mm–100 m
Earth science	1–10 m
Earth observation/remote sensing	1–10 m

The GPS-based system uses a navigation filter (e.g., the EKF) to processes the GPS signal (raw data, Doppler data, and time reference) to determine the relative position and velocity; it provides accuracies that range from meter to millimeter and from centimeters per second to millimeters per second for the relative position and velocity, respectively, depending on implemented algorithm for filtering and onboard autonomy level [19]. It is obvious that this system requires a cooperative target and is only available in Earth orbit.

RF-based systems uses a RF signal, commonly in S, Ku, Ka, and L bands, to estimate, through the implementation of a navigation filter, the range and range rate between spacecraft. The RF-based ranging system relies on a signal modulation technique called the direct sequence spread spectrum (DSSS). The DSSS uses a periodic high rate pseudorandom noise waveform to spread a low rate data signal modulated on a carrier wave over a wider bandwidth [19]. The RF-based navigation system consists of one transmitter, one receiver, and several antennas to enable the coarse-mode intersatellite distance estimation (meter level) based on pseudorange measurements, fine-mode distance (centimeter level), and line-of-sight estimation (subdegree level) based on carrier phases in addition to pseudorange. Within this navigation system class, the FFRF is the only one ever flown: it was developed by TAS France, TAS Spain, and GMV; and it qualified on the PRISMA mission (see Sec. II.C.3). It was designed to provide ranging and LOS measurements for up to four satellites and for an operational range from 10 m to 10 km. This can achieve accuracies better than 1 cm alongtrack and of about 33 cm crosstrack below a 1 km distance (for more details about the FFRF performance, we address the reader to [19] chapter 6). Let us point out that the RF-based systems provide an accuracy that depends on the range between the spacecraft.

Radar systems provide the range and range rate by measuring the phase difference and the Doppler shift between the transmitted and the echo signals. They are also capable of providing the LOS measurement by measuring the delay or phase shift between signals received by two antennas mounted on a baseline at a given distance. This class of sensors is generally used during far-range rendezvous operations (maximum range of 100 km), providing a meter-level accuracy.

The vision-based system is a promising technology for relative navigation and attitude determination. It mainly consists of a camera and, in the case of active system, of a series of LEDs that illuminate some retroreflectors conveniently installed on the tracked spacecraft. These systems generally use techniques and algorithms capable of extracting features of the tracked satellite (such as binarization, contour mapping, and edge detection) in order to set up the synthetic information to determine the relative pose. The estimation of the relative position and velocity is obtained by processing the camera output into a filtering algorithm, together with the dynamics model [19]. An example of this type of system is the VBS system installed on board the PRISMA mission (see Sec. II.C.3).

Laser systems use the same principles of RF sensors. A signal is transmitted by an emitter generally installed on the maneuverable satellite, and the reflected signal is then captured back to determine the range and the LOS. The main difference in technology is given by the wavelength of the electromagnetic signal. In fact, for this type of instrument, the wavelength of the emitted signal is in the near-infrared length on the order of 1000 nm, depending on the available laser diode technology. The relative distance is determined either by measuring the time of flight for the pulse laser system or by the shift of phase of the returning signal for the continuous wave laser range finder. The LOS angle to the target can also be determined by scanning the laser beam and measuring the angle at which a return signal is received [61]. Moreover, optical reflectors on tracked spacecraft are needed to reflect back the laser beam. The typical operating range varies from less than 1 m to a few kilomenters. This system can provide an accuracy from a few millimeters to about 30 mm, depending on the measurement principle, i.e., continuous or pulsed laser signal. The main drawbacks for this system are the high cost, mass, and power consumption as compared to other relative sensors. Note that a filtering process is needed to determine the relative position and velocity from the range and LOS measurements, as it is for the other systems.

Table 8 Sensors for relative navigation used in FF missions

Sensor	Measurements	Achievable accuracy	Remarks
GPS-based system	Relative position Absolute position	mm–cm	Earth missions Cooperative target required
RF-based system	Range Range rate LOS	cm–m	Cooperative targets (transceiver, antennas on target)
Radar system	Range Range rate LOS	m	Uncooperative or cooperative targets
Vision-based system	Range LOS Relative attitude	μm-mm	Cooperative (patterns, LEDs) or uncooperative targets (shape known and complex image processing) Illumination constraints Specific algorithm for the features extracting are required
Laser-based system	Range LOS Relative attitude	mm	Retroreflectors on target for better performances High mass, cost, power Relatively short operative range

Table 8 summarizes the main features of the aforementioned navigation systems and reports the order of magnitude of achievable accuracy with respect to the state of the art of technology.

D. Development Lines in GNC Design

In Sec. II.B, we presented the main technological trends for future FF missions and briefly discussed the impact that these trends might have on the GNC design. Consequently, hereafter, we discuss the areas correlated to GNC design in which researchers should concentrate their efforts to accomplish the challenges posed by the next generation of FF missions.

1. Relative Dynamics Modeling

As discussed in Sec. II.B, both the growing need of onboard autonomy and the requirement of high dynamic range will imply the development of high-accuracy techniques for the orbit control and relative navigation solutions, as well as computationally efficient methods for the determination of guidance profile. To date, the onboard GNC system is mainly based on a linear relative dynamics model, including the perturbations due to the Earth oblateness and atmospheric drag at most [7,22]. However, in order to respond to the increasing demand of high performance, more accurate models should be investigated. For example, the guidance/control solution for impulsive maneuvering of a formation operating in the HEO regime might take advantage of the inclusion in the dynamics model of solar radiation pressure (SRP) and third-body perturbations from the sun and moon. In this scenario, in fact, the magnitude of relative acceleration due to J2/J3 perturbation decreases, getting closer to relative accelerations caused by the aforementioned perturbations. This means that, to accurately describe the relative motion in the HEO regime, SRP and third-body perturbations cannot be ignored. Analogous considerations might be done for the missions operating in the LPO regime. In addition, the formulation of such a more accurate relative dynamics model has to allow the derivation of an associated analytical solution (i.e., the computation of an associated STM and input matrix) to keep the computational load of GNC functions low. For instance, the STM can be used to efficiently propagate the covariance and the trajectory in the prediction step of a Kalman filter. In this way, the inclusion of perturbations in the dynamics model will greatly enhance the filter accuracy without affecting the computational performance.

2. Navigation System

As widely discussed in previous sections, GPS-based systems have been used for relative navigation in many FF missions because they provide high accuracy, robustness, and flexibility, with a relatively low acquisition cost. However, the performance in terms of navigation accuracy lowers when spacecraft operate in an orbital regime different from LEO, such as the HEO regime (about 30 cm at a radial distance of up to 17 Earth radii [62]), as they are not compatible with the future high-accuracy requirements (see Sec. II.B). In addition, this type of system cannot be exploited for those missions planned to fly in the LPO regime. In light of this, other systems such as the optical sensor and laser interferometer should be used to guarantee the required metrology performance in the aforementioned orbital regimes. Let us remark that a video-based system can also be used with a noncooperative target and, more than the laser system, it is compatible with the low-power constraints posed by the use of a small satellite. Thus, it is a promising alternative for the relative navigation for future FF missions. Recently, a video-based system has been tested in orbit during the ARGON experiment, performed in the PRISMA mission (see Sec. II.C.3 for more details). However, this system shall be validated, in terms of the hardware and algorithm for feature extraction, to operate in the HEO and LPO environments.

3. Orbit Control

The use of small satellites for FF missions entails lower available onboard power and thrust levels. For example, the mDOT mission, which is the dual-spacecraft telescope proposed by SLAB at Stanford University [14], foresees the use of a cold-gas propulsion system (VACCO Industries micropropulsion system[¶]) capable of providing a maximum thrust of 25 mN for its main configuration or, alternatively, of the electrospray system (Busek electrospray thruster[**]) able to provide a maximum thrust of 1 mN. To cope with the decrease of thrust level available on board for future FF missions, more efficient orbit control techniques should be developed that allow combining the continuous-thrust and impulsive solutions for maneuvering in order to satisfy the low-thrust constraints, without renouncing high-accuracy performance, and to meet the robustness/flexibility requirements due to the growing onboard autonomy. The authors of this paper have already investigated a hybrid solution using optimal control theory and the primer vector approach [15]; currently, they are studying a more complex method for relative motion control based on the combination of input shaping filtering theory and primer vector theory to get a semianalytical optimal solution that satisfies the low-thrust constraint while guaranteeing high accuracy and robustness, facilitating its onboard implementation.

IV. Conclusions

In this paper, more than 35 formation flying missions were reviewed in order 1) to determine the state of the art of the onboard guidance, navigation, and control (GNC) subsystem in terms of technologies (hardware and software) and achievable performances, and 2) to identify the new trends for this class of missions and how these affect the design of GNC. In addition, the main development

[¶]Data available online at http://www.vacco.com/images/uploads/pdfs/MicroPropulsionSystems_0714.pdf [retrieved 13 September 2016].

[**]Data available online at http://www.busek.com/technologies__espray.htm [retrieved 13 September 2016].

lines for the GNC subsystem required to achieve the challenges posed by the next generation of formation-flying missions were discussed. From the presented survey, it turned out that the most strict requirements in terms of control and navigation performances are associated with the space science missions; for this class of formation-flying missions, centimeter- and millimeter-level accuracies are needed for control and navigation, respectively (control accuracy range of 0.1–10 cm, navigation accuracy range of 1 mm–100 m). Moreover, three key aspects emerged: future missions will 1) require more onboard autonomy, 2) require higher dynamic range performance, and 3) exploit a smaller satellite bus to accomplish their goals. These technological trends pose new challenges for the design of the GNC system, mainly related to the development of robust and accurate methodologies for the orbit control and relative navigation, as well as computationally efficient techniques for the guidance. In light of the aforementioned, the development lines were identified in the GNC system design for the areas of dynamics modeling, orbit control, and the navigation system. New relative dynamics models that allow the inclusion of orbital perturbations, such as solar radiation pressure and third body from (at least) the sun and moon, and the determination of associated analytical solutions to improve the performance of the guidance and filtering process should be investigated. In addition, efficient orbit control techniques capable of combining the continuous-thrust and impulse solutions for spacecraft maneuvering in order to satisfy the low-thrust constraints and to meet the robustness/flexibility requirements due to the growing onboard autonomy should be developed. Ultimately, a video-based system (hardware and software) should be validated and tested to work on board of vehicles operating in the HEO and LPO regimes.

Appendix: Reviewed FF Missions

Table A1 Summary of reviewed FF missions[a,b]

No.	Launch year	Mission	Leading organization	Objective	References
1	2000	CLUSTER	NASA (U.S.), ESA (Europe)	To study the interaction between the solar wind and the Earth's magnetosphere.	[63,64]
2	2002	GRACE	DLR (Germany), NASA (U.S.)	To derive global high-resolution models of the mean and the time-variable components of the Earth's gravity field.	[16–19,21,65]
3	2006	Japan Canada joint collaboration SATellites–Formation Flying	Canadian Space Agency (Canada)	To demonstrate the viability of a space technology qualifying system based on microsatellite (Autonomous Formation Flight experiment with aerodynamic drag control and GPS-based relative navigation).	[66]
4	2010	TanDEM-X	DLR (Germany)	Generation of a global, consistent, timely and high-precision DEM of the Earth.	[19,23,24,31,67]
5	2010	Formation autonomy spacecraft with thrust, Relnav, attitude and crosslink	University of Texas (U.S.)	To investigate enabling technologies crucial for satellite formations, including on-orbit microthrust capability, relative navigation, attitude determination, and satellite crosslink communications.	[68]
6	2010	PRISMA	Swedish Space Corporation (Sweden)	To perform GNC and sensor technology experiments for future formation-flying missions.	[34–36,40,41,69–71]
7	2011	Gravity recovery and interior laboratory	NASA (U.S)	To measure the moon's gravity field in unprecedented detail.	[72]
8	2011	Formation for atmospheric science and technology demonstration	Technical University of Delft (TU Delft; The Netherlands) and Tsinghua University of Beijing (China)	To demonstrate autonomous formation flying using various communication architectures with distributed propulsion systems and Micro ElectroMechanical Systems technology.	[19]
9	2011	Dynamic Ionosphere CubeSat Experiment	ASTRA, LLC (U.S.), Utah State University/Space Dynamics Laboratory (U.S.), Embry–Riddle Aeronautical University (U.S.), Clemson University, Clemson (U.S.)	To map the geomagnetic SEDb plasma bulge and plume formations in Earth's ionosphere.	[73]
10	2012	AeroCube-4	The Aerospace Corporation (U.S.)	To demonstrate formation rephasing using atmospheric drag and deployable wings.	[74,75]
11	2012	HummerSat-1	DFH Satellite Company, Ltd. (China)	To demonstrate the capability of close formation-flying technologies such as relative navigation, guidance and control, intersatellite crosslink, and command.	[76]
12	2012	Shi Jang-9	China National Space Administration (China) Chinese Academy of Space Technology (China)	To demonstrate the functionality of a range of newly developed formation-flying techniques and components.	[77]
13	2013	Focused investigations of relativistic electron burst intensity, range, and dynamics	Montana State University (U.S.), University of New Hampshire (U.S.), The Aerospace Corporation (U.S.), and Los Alamos National Laboratories (U.S.)	To study the properties of so-called "relativistic electron microbursts."	[78]

Table A1 (*Continued.*)

No.	Launch year	Mission	Leading organization	Objective	References
14	2014	Automated navigation and guidance experiment for local space	U.S. Air Force Research Laboratory	To evaluate techniques for detection, tracking, and characterizing of space objects, as well as attribution of actions in space.	[79]
15	2014	CanX-4/CanX-5	University of Toronto, Institute for Aerospace Studies/Space Flight Laboratory (Canada)	To demonstrate formation-flying technology such as differential GPS techniques for high-accuracy relative position determination, fuel-efficient algorithms, and autonomy in maintenance of dual-formation high-accuracy control systems.	[43–46,80]
16	2015	FIREBIRD-II	Montana State University (U.S.), University of New Hampshire (U.S.), The Aerospace Corporation (U.S.), and Los Alamos National Laboratories (U.S.)	See FIREBIRD mission.	[81]
17	2015	MMS	NASA (U.S)	To investigate the physics of magnetic reconnection.	[49,50,82,83]
18	2015	Tianwang-1	Nanjing University of Aeronautics and Astronautics (China)	To demonstrate formation flying and intersatellite communication between three satellites.	[84]
19	2016	Autonomous assembly of a reconfigurable space tele-scope	California Institute of Technology (U.S.), and Surrey Space Centre of the University of Surrey (U.K.)	To demonstrate the hardware and techniques needed to autonomously assemble a reconfigurable space telescope in orbit.	[85]
20	2016	AeroCube 7-Optical Communication and Sensor Demonstration	The Aerospace Corporation (U.S.)	To demonstrate communications and proximity operations capabilities for CubeSats and other spacecraft.	[86]
21	2016	SENTINEL-1A/1B	ESA (Europe)	To provide Copernicus program (previously known as Global Monitoring for Environment and Security) and national services with SAR data for land and ocean monitoring.	[87]
22	2016	Jason-3/2	National Oceanic and Atmospheric Administration (U.S.), European Organization for the Exploitation of Meteorological Satellites (Europe), Centre National d'Etudes Spatiales (France)	To provide ocean surface topography measurements.	[88]
23	2016	BIROS/BEESAT-4 (AVANTI experiment)	DLR (Germany), Technical University of Berlin (Germany)	To demonstrate the feasibility of autonomous, fuel-efficient, and safe proximity operations.	[53–55,89]
24	2016	CubeSat Astronomy by NASA and Yonsei using Virtual telescope ALignment eXperiment	NASA (U.S.) A, Korea's Yonsei University (Republic of Korea) and Korea Aerospace Research Institute (Republic of Korea)	To validate technologies that allow two spacecraft to fly in formation along an inertial line of sight (i. e., align two spacecraft to an inertial source).	[90]
25	2016	DelFFI	TU Delft (The Netherlands)	To characterize low thermosphere with enhanced scientific return by using distributed observation on various geometric baselines and demonstrate autonomous formation flying using various GNC architectures.	[91]
26	2016	CubeSat proximity operations demonstration	Tyvak Inc. (U.S.)	To demonstrate various rendezvous, proximity operations, and docking scenarios in order to validate and characterize several miniature low-power avionics technologies for application to future NASA missions.	[92–96]
27	2016	Space autonomous mission for swarming and geolocation with nanosatellites	Israel Institute of Technology/Distributed Space Systems Laboratory (Israel)	To demonstrate long-term autonomous cluster flight of multiple satellites and determine the position of a cooperative terrestrial emitter based on time difference of arrival and/or frequency difference of arrival.	[97]
28	2017	Prox-1	Georgia Institute of Technology (U.S.)	To demonstrate proximity operations for space situational awareness through the use of a low-thrust propulsion system for orbital maneuvering, as well as visible and infrared imaging for reconnaissance.	[98]
29	2018	XEUS	NASA (U.S.), ESA (Europe)	To provide a large-aperture x-ray telescope combined with high spectral and time resolution instruments, capable of investigating matter under extreme conditions and the evolution of the early universe.	[99,100]
30	2018	Rascal (St. Louis University- 04)	St. Louis University (U.S.)	To demonstrate key technologies for proximity operations and space situational awareness such as infrared imaging, 6DOF propulsion, RF proximity sensing, and automated operations.	[101]

Table A1 (*Continued.*)

No.	Launch year	Mission	Leading organization	Objective	References
31	2019	PROBA-3	ESA (Europe)	To demonstrate technologies and techniques for highly precise satellite formation flying.	[4,102,103]
32	2025	EXO-S	NASA (U.S.)	Space telescope to discover and analyze terrestrial extrasolar planets.	[9]
33	2025	Stellar Imager	NASA (U.S.)	To study solar and stellar magnetic activities and their impact on space weather, planetary climates, and life.	[10,104]
34	TBD	Milli-Arc-second structure imager	NASA (U.S.)	X-ray space telescope to study black holes.	[105]
35	TBD	mDOT	Stanford University/Space Rendezvous Laboratory NASA (U.S.)	To study exozodiacal dust and exoplanets by direct imaging methods while demonstrating the technology readiness of a miniaturized occulter/telescope spacecraft pair.	[14]
36	TBD	SULFRO	Chinese Academy of Space Technology (China)	Ultra-low-frequency observatory to study the history of the dark age.	[12]
37	TBD	SWIFT	JPL (U.S.)	To investigate the formation-flying technologies when an enormous number (1000 or more) of femtosatellite spacecraft is exploited.	[11,106]

[a]U.S. denotes the United States.
[b]SED denotes storm-enhanced density.

Table A2 Summary of GNC features for reviewed missions

Mission	Dynamical model for guidance	Controller type	Required control accuracy	Navigation system	Required navigation accuracy
TerraSAR-X and TanDEM-X	e/i vector separation using ROEs [24].	Impulsive control in pairs of maneuvers to maintain desired relative orbit, using algorithm described in [24,32]. The propulsion system is detailed in Sec. II.C.2.	20 m in radial and crosstrack directions, and 200 m in alongtrack [19]	The navigation hardware is detailed in Sec. II.C.2. A least-squares batch (ROD) adjustment of position and velocity, drag coefficient, solar radiation coefficient, extended maneuvers, and measurement biases is performed to derive the orbit product for formation monitoring and control purposes. The ROD process uses the processed TOR-IGOR data.	Absolute position accuracy: 10 cm; relative position accuracy: 0.5 m crosstrack and 1 m alongtrack.
PRISMA	e/i vector separation with relative orbital elements [36].	Different approaches are implemented, depending on the executed experiment during the mission: mainly impulsive, linear quadratic regulator, and model predictive controllers (Sec. II.C.3). The propulsion system is detailed in Sec. II.C.3.	<25 m at distances of 100 to 2000 m [41]	The navigation hardware is detailed in Sec. II.C.3. The GPS navigation algorithm computes the relative state by differencing the two absolute states through an EKF [71]. The vision-based navigation system uses a kinematic approach, and it determines the range and line of sight during approach with the aid of LEDs [69].	GPS system: relative position and velocity accuracy <3 m and <1 cm/s; relative position and velocity accuracy <0.1 m and <0.2 mm/s [71]. Ground-in-the-loop relative position accuracy <1 cm [40]. VBS system: at far range (1000 km) accuracy is 30 m, and at close range (5 m), accuracy increases to 0.5 mm [69].
CanX-4 and -5	For both ATO and PCO configurations, the guidance trajectories are the periodic solutions to the HCW equations.	Formation-keeping system: FIONA linear state feedback control law with gain matrix developed from LQR method. Pulsewidth modulation strategy used [46]. Reconfiguration system: Relative motion STM-based algorithm to determine fuel-optimal maneuvers [45]. The propulsion system is detailed in Sec. II.C.4.	Relative position <1 m [43]	The navigation hardware is detailed in Sec. II.C.4. The navigation system uses an extended Kalman filter for coarse and fine modes of GPS-based estimation [45].	Absolute position accuracy: coarse 2–5 m, fine 2–5 cm. absolute Velocity accuracy: coarse: 5–10 cm/s, fine: 1–3 cm/s [80]. Relative position accuracy: <10 cm [43].

Table A2 (*Continued.*)

Mission	Dynamical model for guidance	Controller type	Required control accuracy	Navigation system	Required navigation accuracy
MMS	A predetermined velocity change profile uploaded to the spacecraft before each maneuver in the form of a piecewise linear lookup table (velocity in ECIJ2000 versus spacecraft time) is used as guidance [50].	Velocity control: Classic tracker responsible for mapping velocity commands to appropriate thrusters. [49]. The propulsion system is detailed in Sec. II.C.5.	Absolute position error <100 km with 99% probability; relative position error between any two spacecraft <1% scalar separations or 100 m with 99% probability [107].	The navigation hardware is detailed in Sec. II.C.5. The navigation system uses GPS L1 pseudorange measurements and processes them through GEONS software. This uses an EKF to estimate the spacecraft's position, velocity, clock bias with respect to GPS time, clock bias rate, and clock bias acceleration. The GEONS implements a high-fidelity dynamical model including the effects of Earth oblateness, atmospheric drag, solar radiation pressure, the gravity of near bodies, and high-resolution thrust acceleration measurements from the onboard accelerometer [51].	The absolute orbital positions have to be known to within 100 km, root sum squares; whereas the separation distance between the spacecraft has to be known to within the greater of 1% or 100 m (science phases). The onboard orbit determination system has to provide absolute and relative orbit solutions with mean SMA accuracies of 50 and 70 m, respectively, for regions above three RE.
BIROS/AVANTI	A linearized dynamical model, taking into account drag and J2 perturbations, is exploited. An optimal control problem is solved to determine the location of impulsive maneuvers and the associated variation of ROEs to minimize the fuel consumption [57].	The magnitude and the maneuvers required to achieve the precomputed ROE discontinuities are scheduled in the permissible time slots by exploiting a fully analytical four-burn maneuvering scheme (i.e., three in-plane and one out-of-plane maneuvers) that locally guarantee the delta-V minimization [60]. The propulsion system is detailed in Sec. II.C.6.	Control errors: <5 m for relative semimajor axis ($a\delta a$), <15 m for relative inclination and eccentricity vector components, and <100 m for mean relative longitude $a\delta\lambda$ [54].	The navigation hardware is detailed in Sec. II.C.6. The vision-based navigation system adopts a kinematic approach to identify the target satellite and uses the DBSCAN algorithm to isolate spots on images indicating the trajectory of the target satellite. The line-of-sight measurements are sent to an extended Kalman filter [55].	Relative navigation accuracy set to within 10 m for all ROEs except for the mean argument of latitude [54]. Relative orbit determination accuracy <10% range to target.
GRACE	Throughout the mission, the satellites are kept on coplanar orbits within 170–270 km of each other [19].	Both spacecraft are ground controlled. An analytical model is used to plan the maneuvers to meet the aforementioned requirements (see Sec. C.1). The propulsion system is detailed in Sec. II.C.1.			Individual semimajor axes must be determined with accuracy <1 m for maneuver planning [19].

Acknowledgments

The authors would like to acknowledge the U.S. Air Force Research Laboratory, Space Vehicles Directorate, for sponsoring this investigation under contract FAA9453-16-C-0029. The authors wish to thank S. D'Amico of the University of Stanford for his support in the presented survey of guidance, navigation, and control systems for formation-flying missions.

References

[1] Scharf, D. P., Hadaegh, F. Y., and Ploen, S. R., "A Survey of Spacecraft Formation Flying Guidance and Control (Part 1): Guidance," *American Control Conference*, Vol. 2, IEEE Publ., Piscataway, NJ, 2003, pp. 1733–1739. doi:10.1109/acc.2003.1239845

[2] Scharf, D. P., Hadaegh, F. Y., and Ploen, S. R., "A Survey of Spacecraft Formation Flying Guidance and Control. Part II: Control," *American Control Conference*, Vol. 2, IEEE Publ., Piscataway, NJ, 2003, pp. 1733–1739. doi:10.1109/acc.2003.1239845

[3] Bandyopadhyay, S., Subramanian, G. P., and Foust, R., "A Review of Impending Small Satellite Formation Flying Missions," *53rd AIAA Aerospace Sciences Meeting*, AIAA Paper 2015-1623, 2015. doi:10.2514/6.2015-1623

[4] Llorente, J. S., Agenjo, A., Carrascosa, C., de Negueruela, C., Mestreau-Garreau, A., Cropp, A., and Santovincenzo, A., "PROBA-3: Precise Formation Flying Demonstration Mission," *Acta Astronautica*, Vol. 82, No. 1, 2013, pp. 38–46. doi:10.1016/j.actaastro.2012.05.029

[5] Buchen, E., "SpaceWorks' 2014 Nano/Microsatellite Market Assessment," *Proceeding of the AIAA/USU Conference on Small Satellites*, Utah State Univ., SSC14-I-3, Logan, UT, Technical Session I: Private Endeavors, 2014.

[6] Agasid, E., Burton, R., Carlino, R., Defouw, G., Dono Perez, A., Karacahoglu, A. G., Klamm, B., Rademacher, A., Schalkwyck, J., Shimmin, R., Tilles, J., and Weston, S., "Small Spacecraft Technology State of the Art," NASA Ames Research Center TP-2015-216648/REV1, 2015.

[7] Alfried, K., Vadali, S. R., Gurfil, P., How, J., and Breger, L., *Spacecraft Formation Flying: Dynamics, Control and Navigation*, Butterworth-Heinemann, Oxford, England, U.K., 2010, Chaps. 1, 5–8.

[8] Kramer, H. J., *Observation of the Earth and Its Environment: Survey of Missions and Sensors*, Vol. 3rd extended ed., Springer–Verlag, Berlin, 1996, pp. 882–883.

[9] "Exo-S: Starshade Probe-Class Exoplanet Direct Imaging Mission Concept," NASA Rept. 15-1155, 2015.

[10] Carpenter, K. G., Schrijver, C. J., Karovska, M., Allen, R., Breckinridge, J., Brown, A., Chen, P., Folta, D., Harper, G., and Hartman, K., et al., "SI—The Stellar Imager. A UV/Optical Deep-Space Telescope to Image Stars and Observe the Universe with 0.1 milli-arcsec Angular Resolution," NASA Rept., 2005, https://hires.gsfc.nasa.gov/si/documents/SI_Report_final_091505_ebook.pdf.

[11] Hadaegh, F. Y., Chung, S.-J., and Manohara, H. M., "On Development of 100-Gram-Class Spacecraft for Swarm Applications," *IEEE Systems Journal*, Vol. 10, No. 2, 2014, pp. 673–684. doi:10.1109/jsyst.2014.2327972

[12] Wu, S., Chen, W., Zhang, Y., Baan, W., and An, T., "SULFRO: A Swarm of Nano-/Micro-Satellite at SE L2 for Space Ultra-Low Frequency Radio Observatory," *Proceeding of the AIAA/USU Conference on Small Satellites*, Utah State Univ., SSC14-III-9, Logan, UT, Technical Session III: Advanced Technologies I, 2014.

[13] Maessen, D., "Autonomous Relative Navigation for Small Spacecraft," Ph.D. Dissertation, Space Engineering Dept., Delft Univ. of Technology, Delft, The Netherlands, 2014. doi:10.4233/uuid:615bcedc-468f-45e5-89e2-c16615312b2a

[14] Kolmas, J., Banazadeh, P., Koenig, A. W., Macintosh, B., and D'Amico, S., "System Design of a Miniaturized Distributed Occulter/Telescope for Direct Imaging of Star Vicinity," *2016 IEEE Aerospace Conference*, IEEE, New York, 2016, pp. 1–11. doi:10.1109/AERO.2016.7500783

[15] Bevilacqua, R., and Romano, M., "Fuel-Optimal Spacecraft Rendezvous with Hybrid On-Off Continous and Impulsive Thrust," *Journal of Guidance, Control, and Dynamics*, Vol. 30, No. 4, 2007, pp. 1175–1178. doi:10.2514/1.27716

[16] Kang, Z., Tapley, B., Bettadpur, S., Ries, J., Nagel, P., and Pastor, R., "Precise Orbit Determination for the GRACE Mission Using Only GPS Data," *Journal of Geodesy*, Vol. 80, No. 6, 2006, pp. 322–331. doi:10.1007/s00190-006-0073-5

[17] Tapley, B. D., Bettadpur, S., Watkins, M., and Reigber, C., "The Gravity Recovery and Climate Experiment: Mission Overview and Early Results," *Geophysical Research Letters*, Vol. 31, No. 9, 2004. doi:10.1029/2004GL019920

[18] Herman, J., and Steinhoff, M., "Balancing, Turning, Saving: Special AOCS Operations to Extend the GRACE Mission," *AIAA SpaceOps 2012 Conference*, AIAA, Reston, VA, 2012. doi:10.2514/6.2012-1275114

[19] Moccia, A., and Renga, A., *Distributed Space Missions for Earth System Monitoring*, edited by E. Moccia, Springer–Verlag, New York, 2013, Chaps. 8, 9, 13, 19, 21, 22.

[20] Kirschner, M., Montenbruck, O., and Bettadpur, S., "Flight Dynamics Aspects of the GRACE Formation Flying," *16th International Symposium on Spaceflight Dynamics*, JPL, 2001.

[21] Montenbruck, O., Kirshner, M., D'Amico, S., and Bettadpur, S., "E/I Vector Separation for Safe Switching of the GRACE Mission," *Aerospace Science and Technology*, Vol. 10, No. 7, 2006, pp. 628–635. doi:10.1016/j.ast.2006.04.001

[22] D'Amico, S., and Montenbruck, O., "Proximity Operations of Formation-Flying Spacecraft Using an Eccentricity/Inclination Vector Separation," *Journal of Guidance, Control, and Navigation*, Vol. 29, No. 3, 2006, pp. 554–563. doi:10.2514/1.15114

[23] Herbert, J. K., "TDX (TanDEM-X: TerraSAR-X Add-on for Digital Elevation Measurement)," *Earth Observation Portal* [online database], https://directory.eoportal.org/web/eoportal/satellite-missions/t/tandem-x [retrieved 13 Nov. 2016].

[24] Ardaens, J. S., D'Amico, S., Kazeminejad, B., Montenbruck, O., and Gill, E., "Spaceborne Autonomous and Ground-Based Relative Orbit Control for the TerraSAR-X/TanDEM-X Formation," *20th International Symposium on Space Flight Dynamics*, NASA/GSFC, 2007.

[25] Montenbruck, O., Wermuth, M., and Kahle, R., "GPS Based Relative Navigation for the TanDEM-X Mission—First Flight Results," *Journal of Institute of Navigation*, Vol. 58, No. 4, 2011, pp. 293–304. doi:10.1002/navi.2011.58.issue-4

[26] Khale, R., Schlepp, B., Aida, S., Kirschner, M., and Wermuth, M., "Flight Dynamics Operations of the TanDEM-X Formation," *AIAA SpaceOps 2012 Conferences*, AIAA, Reston, VA, 2012. doi:10.2514/6.2012-1275094

[27] Montenbruck, O., van Helleputte, T., and Gill, E., "Reduced Dynamic Orbit Determination Using GPS Code and Carrier Measurements," *Aerospace Science and Technology*, Vol. 9, No. 3, 2005, pp. 261–271. doi:10.1016/j.ast.2005.01.003

[28] Dach, R., Hugentobler, U., Fridez, P., and Meindl, M., (eds.), *User Manual of the Bernese GPS Software Version 5.0*, Univ. of Bern, Astronomical Inst., Bern, Switzerland, Jan. 2007, pp. 1–9, pp. 11–47, pp. 139–164, Chaps. 1, 2, 7.

[29] Zhu, S., Reigber, C., and Konig, R., "Integrated Adjustment of CHAMP, GRACE, and GPS Data," *Journal of Geodesy*, Vol. 78, Nos. 1–2, 2004, pp. 103–108. doi:10.1007/s00190-004-0379-0

[30] Kroes, R., "Precise Relative Positioning of Formation Flying Spacecraft Using GPS," Ph.D. Dissertation, Delft Univ. of Technology, Delft, The Netherlands, 2006.

[31] Montenbruck, M., Kahle, R., D'Amico, S., and Ardaens, J.-S., "Navigation and Control of the TanDEM-X Formation," *Journal of the Astronautical Sciences*, Vol. 56, No. 3, 2008, pp. 341–357. doi:10.1007/BF03256557

[32] D'Amico, S., "Autonomous Formation Flying in Low Earth Orbit," Ph.D. Dissertation, Delft Univ. of Technology, Delft, The Netherlands, 2010.

[33] D'Amico, S., Ardaens, J.-S., Gaias, G., Benninghoff, H., and Schlepp, B., "Noncooperative Rendezvous Using Angles-Only Optical Navigation: System Design and Flight Results," *Journal of Guidance, Control, and Dynamics*, Vol. 36, No. 6, 2013, pp. 1576–1595. doi:10.2514/1.59236

[34] Persson, S., Bodin, P., Gill, E., and Jorgensen, J., "PRISMA—An Autonomous Formation Flying Mission," *Proceedings of the ESA Small Satellite Systems and Services Symposium (4S)*, ESA, Noordwijk, The Netherlands, 2006.

[35] Herbert, J. K., "PRISMA (Prototype Research Instruments and Space Mission technology Advancement)," *Earth Observation Portal* [online database], https://directory.eoportal.org/web/eoportal/satellite-missions/p/prisma-prototype [retrieved 13 Nov. 2016].

[36] Berge, S., Jakobsson, B., Bodin, P., Edfors, A., and Persson, S., "Rendezvous and Formation Flying Experiments within the PRISMA In-Orbit TestBed," *Proceedings of the 6th International ESA Conference on Guidance, Navigation, and Control Systems*, ESA Paper ESA SP-606, Noordwijk, The Netherlands, 2006.

[37] D'Amico, S., Gill, E., Garcia, M. F., and Montenbruck, O., "GPS-Based Real-Time Navigation for the PRISMA Formation Flying Mission," *3rd ESA Workshop on Satellite Navigation User Equipment Technologies (NAVITEC)*, ESA, Noordwijk, The Netherlands, 2006.

[38] Koenig, A. W., Guffanti, T., and D'Amico, S., "New State Transition Matrices for Relative Motion of Spacecraft Formations in Perturbed Orbits," *AIAA/AAS Astrodynamics Specialist Conference, SPACE Conference and Exposition*, AIAA Paper 2016-5635, 2016. doi:10.2514/6.2016-5635

[39] Delpech, M., Guidotti, P. Y., Djalal, S., Grelier, T., and Harr, J., "RF Based Navigation for PRISMA and Other Formation Flying Missions in Earth Orbit," *21st International Symposium on Space Flight Dynamics*, CNES, Paris, France, 2009.

[40] D'Amico, S., Ardaens, J.-S., and De Florio, S., "Autonomous Formation Flying Based on GPS—PRISMA Flight Results," *Acta Astronautica*, Vol. 82, No. 1, 2013, pp. 69–79. doi:10.1016/j.actaastro.2012.04.033

[41] Gill, E., D'Amico, S., and Montenbruck, O., "Autonomous Formation Flying for the PRISMA Mission," *Journal of Spacecraft and Rockets*, Vol. 44, No. 3, 2007, pp. 671–681. doi:10.2514/1.23015

[42] De Florio, S., D'Amico, S., and Radice, G., "Flight Results of Precise Autonomous Orbit Keeping Experiment on PRISMA Mission," *Journal of Spacecraft and Rockects*, Vol. 50, No. 3, 2013, pp. 662–674. doi:10.2514/1.A32347

[43] Herbert, J. K., "CanX-4&5 (Canadian Advanced Nanospace eXperiment-4&5)," *Earth Observation Portal* [online database], https://directory.eoportal.org/web/eoportal/satellite-missions/c-missions/canx-4-5 [retrieved 13 Nov. 2016].

[44] Bonin, G., Roth, N., Armitage, S., Newman, J., Risi, B., and Zee, R. E., "CanX-4 and CanX-5 Precision Formation Flight: Mission Accomplished!" *Proceedings of the 29th Annual AIAA/USU Conference on Small Satellites*, Utah State Univ., SSC15-I-4, Logan, UT, Technical Session I: All Systems Go!, 2015.

[45] Roth, N. H., "Navigation and Control Design for the CanX-4/-5 Satellite Formation Flying Mission," M.S. Thesis, Aerospace Science and Engineering Dept., Univ. of Toronto, Toronto, Canada, 2011.

[46] Eyer, J. K., Damaren, C., Zee, R. E., and Cannon, E., "A Formation Flying Control Algorithm for the CanX-4&5 Low Earth Orbit Nanosatellite Mission," *Space Technology*, Vol. 27, No. 4, 2007, pp. 147–158.

[47] Long, A., Farahmand, M., and Carpenter, R., "Navigation Operations for the Magnetospheric Multiscale Mission," *25th International Symposium on Space Flight Dynamics*, DLR/ESA, Oberpfaffenhofen/Darmstadt, Germany, 2015.

[48] Tooley, C. R., Black, R. K., Robertson, B. P., Stone, J. M., Pope, S. E., and Davis, G. T., "The Magnetospheric Multiscale Constellation," *Space Science Reviews*, Vol. 199, Nos. 1–4, 2016, pp. 23–76. doi:10.1007/s11214-015-0220-5

[49] Chai, D. J., Queen, S. Z., and Placanica, S. J., "Precision Closed-Loop Orbital Maneuvering System Design and Performance for the Magnetospheric Multiscale Formation," *Proceedings of the 25th International Symposium on Space Flight Dynamics*, DLR/ESA, Oberpfaffenhofen/Darmstadt, Germany, 2015.

[50] Farahmand, M., Long, A., and Carpenter, R., "Magnetospheric Multiscale Mission Navigation Performance Using the Goddard Enhanced Onboard Navigation System," *25th International Symposium on Space Flight Dynamics*, DLR/ESA, Oberpfaffenhofen/Darmstadt, Germany, 2015.

[51] Queen, S. Z., Chai, D., and Placanica, S., "Orbital Maneuvering System Design and Performance for the Magnetospheric Multiscale Formation," *Proceeding of AAS/AIAA Astrodynamics Conference 2015*, Vol. 156, Univelt Inc., Escondido, CA, 2016.

[52] Queen, S. Z., Benegalrao, S., and Shah, N., "Generalized Momentum Control of the Spin-Stabilized Magnetospheric," *2015 AAS/AIAA Astrodynamics Specialist Conference*, Univelt Inc., Escondido, CA, 2015.

[53] Herbert, J. K., "BIROS (Bi-spectral InfraRed Optical System)," *Earth Observation Portal* [online database], https://directory.eoportal.org/web/eoportal/satellite-missions/b/biros [retrieved 13 Nov. 2016].

[54] Gaias, G., Ardaens, J.-S., and D'Amico, S., "The Autonomous Vision Approach Navigation and Target Identification (AVANTI) Experiment: Objectives and Design," *9th International ESA Conference on Guidance, Navigation and Control Systems*, ESA, Noordwijk, The Netherlands, 2014.

[55] Gaias, G., Ardaens, J.-S., and Terzibaschian, T., "Paving the Way for Future On-Orbit Servicing Missions: The AVANTI Experiment," *25th International Symposium on Space Flight Dynamics*, DLR/ESA, Oberpfaffenhofen/Darmstadt, Germany, 2015.

[56] Gaias, G., D'Amico, S., and Ardaens, J.-S., "Angles-Only Navigation to a Noncooperative Satellite Using Relative Orbital Elements," *Journal of Guidance, Control, and Dynamics*, Vol. 37, No. 2, 2014, pp. 439–451. doi:10.2514/1.61494.

[57] Gaias, G., D'Amico, S., and Ardaens, J.-S., "Generalised Multi-impulsive Manoeuvres for Optimum Spacecraft Rendezvous in Near-Circular Orbit," *International Journal of Space Science and Engineering*, Vol. 3, No. 1, 2015, pp. 68–88. doi:10.1504/IJSPACESE.2015.069361

[58] Gaias, G., and D'Amico, S., "Impulsive Maneuvers for Formation Reconfiguration Using Relative Orbital Elements," *Journal of Guidance, Control, and Dynamics*, Vol. 38, No. 6, 2015, pp. 1036–1049. doi:10.2514/1.G000189

[59] Gill, E., Sundaramoorthy, P., Bouwmeester, J., Zandbergen, B., and Reinhard, R., "Formation Flying Within a Constellation of Nano-Satellites: The QB50 Mission," *Acta Astronautica*, Vol. 82, No. 1, 2013, pp. 110–117. doi:10.1016/j.actaastro.2012.04.029

[60] "X-Ray Observatory: Study Preparation Activities," ESA Status Rept. 2, SCI-AM Rept. SCI-A/2006/188/NR, Noordwijk, The Netherlands, Nov. 2006, pp. 1–29.

[61] Fehese, W., *Automated Rendezvous and Docking of Spacecraft*, Cambridge Univ. Press, New York, 2003, Chaps. 1, 4, 7.

[62] Rupp, T., D'Amico, S., Montnbruck, O., and Gill, E., "Autonomous Formation Flying at DLR's German Space Operations Center (GSOC)," *Proceeding of the 58th International Astronautical Congress*, Curran Associates Inc., Red Hook, NY, 2007.

[63] Credland, J., Mecke, G., and Ellwood, J., "The Cluster Mission: ESA's Spacefleet to the Magnetosphere," *Space Science Reviews*, Vol. 79, No. 1, 1997, pp. 33–64. doi:10.1023/A:1004914822769

[64] Volpp, J., Escoubet, P. C., Foley, S., Godfrey, J., Hapgood, M., and Pallaschke, S., "CLUSTER Constellation Change Manoeuvres—Management and Operations," *Space OPS 2004 Conference*, AIAA, Reston, VA, 2004. doi:10.2514/6.2004-238-91

[65] Kroes, R., Montenbruck, O., Bertinger, W., and Visser, P., "Precise GRACE Baseline Determination Using GPS," *GPS Solutions*, Vol. 9, No. 1, 2005, pp. 21–31. doi:10.1007/s10291-004-0123-5

[66] Herbert, J. K., "JC2Sat-FF (Japan Canada Joint Collaboration Satellites—Formation Flying)," *Earth Observation Portal* [online database], https://directory.eoportal.org/web/eoportal/satellite-missions/j/jc2sat-ff [retrieved 13 Nov. 2016].

[67] Ardaens, J.-S., D'Amico, S., Ulrich, D., and Fischer, D., "TanDEM-X Autonomous Formation Flying System," *Proceedings of the 3rd International Symposium on Formation Flying, Missions and Technologies*, 2008.

[68] Herbert, J. K., "FASTRAC (Formation Autonomy Spacecraft with Thrust, Relnav, Attitude, and Crosslink)," *Earth Observation Portal* [online database], https://directory.eoportal.org/web/eoportal/satellite-missions/f/fastrac [retrieved 13 Nov. 2016].

[69] Jorgensen, J., and Benn, M., "VBS—The Optical Rendezvous and Docking Sensor for PRISMA," *NordicSpace*, 2010.

[70] Jorgensen, J., Delpech, M., Malbet, F., Karlsson, T., Larsson, R., and Leger, A., "Flight Demonstration of Formation Flying Capabilities for Future Missions (NEAT Pathfinder)," *Acta Astronautica*, Vol. 105, No. 1, 2014, pp. 82–94. doi:10.1016/j.actaastro.2014.05.027

[71] Bodin, P., Larsson, R., Nilsson, F., Chasset, C., Noteborn, R., and Nylund, M., "PRISMA: An In-Orbit Test Bed for Guidance, Navigation, and Control Experiments," *Journal of Spacecraft and Rockets*, Vol. 46, No. 3, 2009, pp. 615–623. doi:10.2514/1.40161

[72] Herbert, J. K., "GRAIL (Gravity Recovery and Interior Laboratory)," *Earth Observation Portal* [online database], https://directory.eoportal.org/web/eoportal/satellite-missions/g/grail [retrieved 13 Nov. 2016].

[73] Herbert, J. K., "DICE (Dynamic Ionosphere CubeSat Experiment), DICE-1 and DICE-2," *Earth Observation Portal* [online database], https://directory.eoportal.org/web/eoportal/satellite-missions/d/dice [retrieved 13 Nov. 2016].

[74] Herbert, J. K., "AeroCube-4," *Earth Observation Portal* [online database], https://directory.eoportal.org/web/eoportal/satellite-missions/a/aerocube-4 [retrieved 13 Nov. 2016].

[75] Gangestad, J. W., Hardy, B. S., and Hinkley, D. A., "Operations, Orbit Determination, and Formation Control of the AeroCube-4 CubeSats," *Proceedings of the 27th Annual AIAA/USU Conference on Small Satellites*, 2013.

[76] Herbert, J. K., "HummerSat-1/FN-1 (Fengniao-1A/B)," *Earth Observation Portal* [online database], https://directory.eoportal.org/web/eoportal/satellite-missions/h/hummersat-1 [retrieved 13 Nov. 2016].

[77] Herbert, J. K., "SJ-9 (Shi Jian-9 Formation Flight Mission)," *Earth Observation Portal* [online database], https://directory.eoportal.org/web/eoportal/satellite-missions/s/shi-jian-9 [retrieved 13 Nov. 2016].

[78] Klumpar, D., Springer, L., Mosleh, E., Mashburn, K., Berardinelli, S., and Gunderson, A., et al., "Flight System Technologies Enabling the Twin-CubeSat FIREBIRD-II Scientific Mission," *Proceedings of the AIAA/USU Conference on Small Satellites*, Utah State Univ., SSC15-V-6, Logan, UT, Technical Session V: Year in Review, 2015.

[79] "Automated Navigation and Guidance Experiment for Local Space (ANGELS)," U.S. Air Force Research Lab. Fact Sheet, 2014.

[80] Eyer, J. K., Damaren, C., and Zee, R., "The Guidance and Control Algorithms for the CanX-4&5 Formation Flying Demonstration Mission," *Proceedings of the 3rd International Symposium on Formation Flying, Missions and Technologies*, ESA SP-654, ESA Communication Production Office, 2008.

[81] Klumpar, D., et al., "Flight System Technologies Enabling the Twin-CubeSat FIREBIRD-II Scientific Mission," *Proceedings of the 29th Annual AIAA/USU Conference on Small Satellites*, 2015.

[82] Herbert, J. K., "MMS (Magnetospheric MultiScale) Constellation," *Earth Observation Portal* [online database], https://directory.eoportal.org/web/eoportal/satellite-missions/m/mms-observatory [retrieved 13 Nov. 2016].

[83] Gim, D.-W., and Alfriend, K. T., "Criteria for Best Configuration and Sub-Optimal Reconfiguration for MMS Mission," *Proceedings of the 14th AAS/AIAA Space Flight Mechanics Meeting*, Vol. 119, Univelt Inc., Escondido, CA, 2005, pp. 947–968.

[84] "Tianwang 1C," *NASA Space Science Data Coordinated Archive* [online database], NASA, http://nssdc.gsfc.nasa.gov/nmc/spacecraftDisplay.do?id=2015-051B [retrieved 13 Nov. 2016].

[85] Herbert, J. K., "AAReST (Autonomous Assembly of a Reconfigurable Space Telescope)," *Earth Observation Portal* [online database], https://directory.eoportal.org/web/eoportal/satellite-missions/a/aarest [retrieved 13 Nov. 2016].

[86] Herbert, J. K., "AeroCube 7-OCSD (AeroCube—Optical Communication and Sensor Demonstration)," *Earth Observation Portal* [online database], https://directory.eoportal.org/web/eoportal/satellite-missions/a/aerocube-ocsd [retrieved 13 Nov. 2016].

[87] Herbert, J. K., "Copernicus: Sentinel-1 The SAR Imaging Constellation for Land and Ocean Services," *Earth Observation Portal* [online database], https://directory.eoportal.org/web/eoportal/satellite-missions/c-missions/copernicus-sentinel-1 [retrieved 13 Nov. 2016].

[88] Herbert, J. K., "Jason-3 Altimetry Mission," *Earth Observation Portal* [online database], https://directory.eoportal.org/web/eoportal/satellite-missions/j/jason-3 [retrieved 13 Nov. 2016].

[89] Gaias, G., and Ardaens, J.-S., "Design Challenges and Safety Concept for the AVANTI Experiment," *Acta Astronautica*, Vol. 123, June–July 2016, pp. 409–419.
doi:10.1016/j.actaastro.2015.12.034

[90] Shah, N., and Calhoun, P., "The "Virtual" Space Telescope: A New Class of Science Missions," NASA 2016.

[91] "DelFFi Mission," *Delfi Space* [online database], Delft Univ. of Technology, Delft, The Netherlands, http://www.delfispace.nl/delffi [retrieved 13 Nov. 2016].

[92] Roscoe, C. W. T., Westphal, J. J., Lutz, S., and Bennett, S., "Guidance, Navigation, and Control Algorithms for Cubesat Formation Flying," *Proceedings of the 38th AAS Guidance and Control Conference*, 2015.

[93] Bowen, J., Villa, M., and Williams, A., "CubeSat-Based Rendezvous, Proximity Operations, and Docking in the CPOD Mission," *Proceedings of the 29th Annual AIAA/USU Conference on Small Satellites*, 2015.

[94] Williams, A., "CubeSat Proximity Operations Demonstration (CPOD) Vehicle Avionics and Design," *Tyvak*, 2015.

[95] Bowen, J., Tsuda, A., Abel, J., and Villa, M., "CubeSat Proximity Operations Demonstration (CPOD) Mission Update," *Proceedings of the 2015 IEEE Aerospace Conference*, IEEE Publ., Piscataway, NJ, 2015, pp. 1–8.
doi:10.1109/aero.2015.7119124

[96] Roscoe, C. W. T., Westphal, J. J., Griesbach, J. D., and Schaub, H., "Formation Establishment and Reconfiguration Using Differential Elements in J2-Perturbed Orbits," *Journal of Guidance, Control, and Dynamics*, Vol. 38, No. 9, 2015, pp. 1725–1740.
doi:10.2514/1.G000999

[97] Gurfil, P., Herscovitz, J., and Pariente, M., "The SAMSON Project—Cluster Flight and Geolocation with Three Autonomous Nano-Satellites," *Proceeding of the 26th AIAA/USU Conference on Small Satellites*, 2012.

[98] Spencer, D. A., Chait, S. B., Schulte, P. Z., Okseniuk, K. J., and Veto, M., "Prox-1 University-Class Mission to Demonstrate Automated Proximity Operations," *Journal of Spacecraft and Rockets*, Vol. 53, No. 5, 2016, pp. 847–863.
doi:10.2514/1.a33526

[99] Rando, N., Lyngvi, A., Gondoin, P., Lumb, D., Bavdaz, M., Verhoeve, P., de Wilde, D., Parmar, A., and Peacock, T., "ESA Study of XEUS, A Potential Follow-On to XMM-Newon," *Proceedings of the 6th International Conference on Space Optics*, ESA SP-621, 2006.

[100] Bleeker, J., and Mendez, M., "The XEUS Mission," *Proceedings of the Symposium 'New Visions of the X-Ray Universe in the XMM-Newton and Chandra Era'*, ESA SP-488, 2001.

[101] Gunter, K., "Rascal (SLU 04)," *Gunter's Space Page* [online database], http://space.skyrocket.de/doc_sdat/rascal.htm [retrieved 13 Nov. 2016].

[102] "PROBA-3 Phase A Study Executive Summary Report," *EADS Astrium*, PROBA-3 Phase A Team Rept. PROBA3-ASU-RPT, 2007.

[103] Villien, A., Cavel, C., Morand, J., and Borde, J., "Formation Flying Guidance Navigation and Control Design for Science Missions," IFAC Proceedings Volumes, *Proceedings of the 17th World Congress: The International Federation of Automatic Control*, Vol. 41, No. 2, 2008, pp. 2131–2136.
doi:10.3182/20080706-5-kr-1001.00361

[104] Christensen-Dalsgaard, J., Karovska, M., Carpenter, K. G., Schrijver, C. J., and Karovska, M., "The Stellar Imager (SI)—A Mission to Resolve Stellar Surfaces, Interiors, and Magnetic Activity," *Journal of Physics: Conference Series*, Vol. 271, 2011, Paper 012085.
doi:10.1088/1742-6596/271/1/012085

[105] Skinner, G. K., Arzoumanian, Z., Cash, W. C., Gehrels, N., Gendreau, K. C., Gorenstein, P., Krizmanic, J. F., Miller, M. C., Phillips, J. D., Reasenberg, R. D., Reynolds, C. S., Sambruna, R. M., Streitmatter, R. E., and Windt, D. L., "The Milli-Arc-Second Structure Imager, MASSIM: A New Concept for a High Angular Resolution X-Ray Telescope," *Proceedings of the SPIE*, Vol. 7011, July 2008, Paper 70110T.
doi:10.1117/12.789568

[106] Chung, S.-J., and Hadaegh, F. Y., "Swarms of Femtosats for Synthetic Aperture Applications," *4th International Conference on Spacecraft Formation Flying Missions and Technologies*, 2011.

[107] Bamford, W., Mitchell, J., Southward, M., Baldwin, P., Winternitz, L., Heckler, G., Kurichh, R., and Sirotzky, S., "GPS Navigation for the Magnetospheric Multi-Scale Mission," *Proceedings of the 22nd International Technical Meeting of The Satellite Division of the Institute of Navigation*, Inst. of Navigation (ION), Manassas, VA, 2009, pp. 1447–1457.